RSC Advances

PAPER

View Article Online
View Journal | View Issue

Cite this: *RSC Adv.*, 2020, **10**, 31961

Quercetin loaded folate targeted plasmonic silver nanoparticles for light activated chemo-photothermal therapy of DMBA induced breast cancer in Sprague Dawley rats†

Pritha Bose,[a] Amiya Priyam,[b] Rajiv Kar[c] and Shakti P. Pattanayak *[ad]

Currently, the paucity of free drugs in conventional chemotherapy for breast-cancer curbs the desired therapeutic efficiency, often aggravating systemic toxicity. Quercetin (QRC) is a potential chemotherapeutic bio-flavonoid that is associated with poor hydrophilicity. In contrast to spherical silver nanoparticles (AgNPs), anisotropic AgNPs exhibit prominent plasmonic tunability in the near infrared (NIR) region allowing deep tissue penetration and endowing them with the ability to act as photothermal transducers as well. In this study, we optimized a simple and novel method for synthesizing folate-receptor-targeted-plasmonic silver-nanoparticles (QRC-FA-AgNPs) to serve as an efficient nanoscopic carrier system for breast cancer-cell targeted delivery of QRC and to induce photothermal therapy. A one-pot chemical synthesis method was followed for synthesizing the QRC-FA-AgNPs by finely tailoring the hydrogen bond between the reductant and stabilizer. Detailed characterization through UV-visible, near infrared (UV-vis-NIR) spectroscopy, Fourier transform infrared (FTIR), X-ray diffraction (XRD), transmission electron microscopy (TEM), selected area electron diffraction (SAED), and energy-dispersive X-ray spectroscopy (EDX), along with particle-size, zeta-potential analysis, drug-loading and release capacity and stability studies were also performed. *In vitro* targeted cellular uptake, viability studies, chemo-photothermal efficacy, induction of apoptosis and the reactive oxygen species (ROS) generating potential were studied in the MDA-MB-231 cell-line and *in vivo* evaluation of the chemo-photothermal efficacy of QRC-FA-AgNPs was performed using a 7,12-dimethylbenz(*a*)anthracene (DMBA)-induced breast-carcinogenesis model in Sprague Dawley rats. Unlike conventional AgNPs, these novel pentagonal QRC-FA-AgNPs (<50 nm) manifested a robust plasmon tunability in the NIR (>800 nm) region. Detailed *in vitro* and *in vivo* studies revealed their active role in improving breast-cancer conditions by allowing controlled and targeted discharge of QRC at the tumor site, along with evoking hyperthermia under NIR laser irradiation that induced selective ablation of cancer cells. Following successful cellular internalization, the photothermal efficacy of QRC-FA-AgNPs supplemented their chemotherapeutic potency, allowing apoptosis and restraining the tumor growth. This current study highlighted the augmented efficacy of plasmonic QRC-FA-AgNPs in comparison to free quercetin, thus the development of a potential nanocarrier based on the pleiotropic function of plasmonic AgNPs may provide an efficient combined chemo-photothermal based strategy for the assassination of breast-cancer cells.

Received 2nd July 2020
Accepted 12th August 2020

DOI: 10.1039/d0ra05793b

rsc.li/rsc-advances

1. Introduction

Breast cancer, categorized as one of the most frequent and prevalent malignancies among women, is the second leading cause of mortality following lung cancer. In 2019, it was estimated that about 268 600 new breast cancer (invasive) cases were diagnosed in women, with 41 760 expected to result in death.[1] The limitations of conventional chemotherapy characterize it as an unsatisfactory therapeutic strategy for such a life-threatening disease. Poor biodistribution of the standard chemotherapeutic agents, along with their non-specific tumor

[a]*Division of Advanced Pharmacology, Department of Pharm. Sciences & Technology, Birla Institute of Technology, Mesra, Ranchi-835215, India*

[b]*Department of Chemistry, School of Physical and Chemical Sciences, Central University of South Bihar, Gaya 824236, India*

[c]*Fritz Haber Centre for Molecular Dynamic Research, Hebrew University of Jerusalem, Israel*

[d]*Department of Pharmacy, School of Health Sciences, Central University of South Bihar, Gaya-824209, India. E-mail: sppattanayak@cusb.ac.in; profsppattanayak@gmail.com; Tel: +91-9123240698*

† Electronic supplementary information (ESI) available. See DOI: 10.1039/d0ra05793b

delivery result in undesirable side effects to normal tissues and fosters an inadequate dosage to destroy the cancer cells.[2,3] Moreover, as a greater amount of cancer cells are being recognized as being multidrug resistant, the insufficiency of the single therapy mode is becoming more apparent. Such a scenario demands prompt use of targeted[4–6] and combined treatment options[7–9] to improve therapeutic efficiency and biosafety for the treatment of breast cancer. This paradigm shift has thus created a profound impact on the current research that now focuses on the discovery of newer bioactive phytoconstituents and advances in the field of nanotechnology. In this context, nanoparticles, as efficient drug delivery cargos, serve as an encouraging anti-cancer therapeutic approach.

Quercetin (QRC), a potent bioflavonoid which is abundantly available in plants and in the human diet (*e.g.* onion, lettuce, tea, red grapes, tomatoes *etc.*), is reported to possess diverse pharmacological properties, as well as toxic effects towards various cancer cells.[10–12] Studies have documented QRC to influence a number of key effectors in different signal transduction cascades associated with intrinsic apoptosis[13] and cell cycle arrest in breast cancer cells.[11,13] However, the insufficient aqueous solubility of QRC accounts for its poor bioavailability (20%, as shown by its water-soluble derivative), which in turn impedes its chemotherapeutic potential and also means that higher doses of QRC need to be administrated for clinical application.[12,14–16]

To surpass these obstacles and further enhance the efficacy of QRC, nano-formulations may be improvised to provide a successful platform for combining multiple therapeutic and/or diagnostic modalities.[17] The nanoscale size (smaller than human cells by approximately 100–1000 times) facilitates their interactions with various biomolecules, which contributes to the unprecedented outcome of accurate therapy, as well as diagnosis.[18] Anisotropic silver nanoparticles (AgNPs), among different relevant nanoparticles (NPs), have gained significant attention owing to their robust plasmon tunability in the biologically transparent window of 650–1200 nm.[19] According to various studies, AgNPs have been identified to be genotoxic and are also attributed to antitumor activities *in vitro* and *in vivo*.[20,21] AgNPs are also responsible for the selective killing of cancer cells by reactive oxygen species (ROS) induced apoptosis (mitochondria dependent).[22,23] Moreover, the efficiency of AgNPs in cancer therapy is significantly escalated by virtue of its photothermal effect.[24,25] Distinctive near infrared (NIR) excitation from a laser source ensures superior tissue permeability and promotes luminous-to-heat conversion at the tumor region that invokes hyperthermia (>41 °C) and is termed photothermal therapy (PTT).[24,26] The resultant heat allows selective killing of tumor cells without damaging healthy tissues because of the variation in the thermal tolerance between them.[25] PTT is therefore an effective anticancer therapeutic modality owing to its non-invasive properties.[27–29] In recent years, extensive nanoscale research has been primarily focused on unveiling the efficiency of diversified engineered nanoparticles including molybdenum disulfide (MoS_2)-keratin nanosheets,[30] gold coated liposomes,[31] reduced graphene-polyallylamine hydrochloride nanocomposites,[32] nanoceria-molybdenum nanoflakes,[33] and so forth for inducing and improving photothermal therapy against liver, breast and other cancers. Thus, these "optically hot" anisotropic AgNPs can serve as a multifunctional drug delivery system facilitating combined chemo-photothermal therapy. As folate receptors (FR) are highly over-expressed in breast and other cancers,[34] with respect to normal tissues, folic acid (FA) is therefore considered to be a tumor targeting molecule for breast cancer theranostics owing to its high binding affinity towards FR. Accordingly, developing a high performance FA functionalized nanocarrier may authorize targeted cancer cell endocytosis and accumulation allowing superior biocompatibility for practical utilization of AgNPs based PTT for breast cancer.

Thus, in contrast to the complex multistep methods previously reported, in this study, we optimized a simple, novel and one-pot chemical synthesis technique for formulating a FR targeting silver based plasmonic nanocarrier for escalating the potency of QRC. Also, detailed *in vitro* and *in vivo* investigations were performed to evaluate the breast cancer specific cell targeting ability with the combined chemo-photothermal efficacy of QRC-FA-AgNPs against breast cancer. Among the various preclinical rodent models explored for breast cancer studies, we opted for DMBA (7,12-dimethylbenz(*a*)anthracene), a prototype of polyaromatic hydrocarbons (PAH), induced breast cancer model on Sprague Dawley rats[35,36] for the *in vivo* evaluations.

2. Material and methods

2.1. Synthesis of plasmonic anisotropic AgNPs

The silver nanoparticles were synthesized according to the method described previously.[19] Briefly, initial mixing of the $AgNO_3$ (1 mM, 10 ml) and citrate (80 mM, 0.5 ml) solution was followed by the addition of hydrazine hydrate (40 mM, 2 ml), the solution was maintained at pH 5 and a temperature of 5 °C with constant stirring until a green color appeared. The pH adjustment of the solution was carried out by adding 1 M NaOH or 1 M H_2SO_4 dropwise.

2.2. Synthesis of folate receptor targeted AgNPs (FA-AgNPs)

In this study we performed a novel and simplified method of folic acid conjugation with AgNPs. The pH of the previously synthesized silver nanoparticle (AgNP) solution (12.5 ml) was adjusted to a pH of 7.6 before adding folic acid solution (160 mM, 0.5 ml) under constant stirring. After that the solution was allowed to rest for 2 h followed by freeze drying to concentrate it to at least one fifth of the previous volume. Isopropyl alcohol (IPA, 10 ml) was added to the sample and then it was centrifuged at 4500 rpm for 10 min. The resulting supernatant was decanted and the obtained pellets were again centrifuged with IPA under similar conditions as previously stated. After the second washing, pellets of FA-AgNPs were collected and lyophilized to a powdered form for further use and characterization.

2.3. Synthesis of QRC quenched folate receptor targeted AgNPs (QRC-FA-AgNPs)

For the quenching of QRC to FA-AgNPs, QRC and FA (1 : 1) were dissolved in Millipore water (using an alkaline pH enables

better solubility) and the pH was adjusted to 11. 0.5 ml of this solution was added to the previously synthesized AgNPs (12.5 ml) which had also been adjusted to a similar pH as that of the QRC + FA solution under constant stirring. Then, after a 2 h resting period, the prepared solution was freeze dried following a previously described method for FA-AgNPs. After being adequately concentrated the solution was centrifuged by adding IPA and washed twice as described previously to obtain the final pellets of QRC-FA-AgNPs. These pellets were then lyophilized, powdered and stored for further characterization.

2.4. Drug (QRC) loading content of the QRC-FA-AgNPs

The QRC loading efficacy of the synthesized AgNPs was calculated using an indirect method of estimating the QRC content of the supernatant in the solution after centrifugation at 10 000 rpm for 30 min. The drug concentration in the supernatant was measured under UV absorbance at 269 nm by using UV-visible spectroscopy (UV-2450, Shimadzu, Kyoto, Japan) and the percentage of loading of QRC in the synthesized AgNPs was estimated using the following formula.

$$\text{Loading efficiency} = \frac{w_o}{w} \times 100$$

In which w_o is the weight of the QRC loaded on the FA-AgNPs and w is the weight of the synthesized FA-AgNPs.

2.5. Characterization of the QRC-FA-AgNPs

Following double dilution of the samples, a UV-2450 (Shimadzu, Kyoto, Japan) spectrophotometer was used to perform UV-vis-near-IR absorption spectroscopy. The possible composition of nanoparticles was determined using Fourier transform infrared (FTIR) spectroscopy (IR-Prestige 21; Shimadzu Corporation, Japan) in a scanning wave number ranging from 400–4000 cm^{-1} at a 2 cm^{-1} resolution following the KBr pellet method. X-ray diffraction (XRD) was carried out to analyze the nature of the synthesized NPs (Rigaku, Japan) while transmission electron microscopy (TEM, FEI-Tecnai G2 20 S-TWIN) was employed to establish the morphological features (size, shape, as well as structure) of the anisotropic nanoparticles which was followed by energy dispersive X-ray spectroscopy (EDX) and selected area electron diffraction (SAED) analysis. For TEM analysis a few drops of the synthesized nanoparticles were placed on copper grids (carbon coated) (Ted Pella, product code: 01800) and dried immediately in a vacuum desiccator. A Zeiss microscope (operating voltage; 200 kV) was used for recording the images and SAED was used to revalidate the crystallinity. In addition, dynamic light scattering (DLS) was performed for determining the average size distribution of the NPs, the polydispersity index and the zeta potential (surface charge) in a Nano ZS Zetasizer (Malvern Instruments Ltd., Malvern, UK) following appropriate dilution of the samples.

The stability of the QRC-FA-AgNPs was evaluated by incubating it in three biologically relevant media such as deionized water, cell culture medium (Dulbecco's modified Eagle's medium (DMEM), glucose and 10% fetal bovine serum (FBS)) and phosphate buffer (PBS) respectively, followed by daily determination of variations in the hydrodynamic diameter and polydispersity index (PDI) (Nano ZS Zetasizer; Malvern Instruments Ltd., Malvern, UK) of the NPs for a period of 14 d.[37]

2.6. Analysis of *in vitro* QRC release from QRC-FA-AgNPs

The dialysis method was implemented to estimate the release of QRC from the synthesized nanoparticles at 37 °C in pH values of 7.4 and 5.5 respectively, corresponding to the physiological systemic environment. Briefly, following 30 min stabilization of QRC-FA-AgNPs (containing drug equivalent 5 mg) suspended in PBS (1 ml), the suspension was placed in a dialysis bag (MW CO 2000 Da; Sigma-Aldrich). The pH of 10 ml of PBS was adjusted to 7.4 and 5.5 with subsequent submersion of the dialysis bag and incubation at 37 °C in a water bath with constant stirring at 130 rpm respectively. At regular and predetermined time intervals 1 ml of PBS was withdrawn and immediately replaced with an equivalent amount of PBS maintained at similar conditions. The withdrawn samples were analyzed using a UV-2450 (Shimadzu, Kyoto, Japan) spectrophotometer at 269 nm. The experiments were performed thrice at individually selected pH values.

2.7. Cell line and cell culture

The human breast cancer (MDA-MB-231) cell lines were purchased from NCCS (National Centre for Cell Science) Pune, India and cultured in DMEM/F12 media supplemented with 10% FBS, streptomycin (100 U ml^{-1}) and penicillin (100 mg ml^{-1}). The cells were maintained in a humidified atmosphere of 5% CO_2 at 37 °C.

2.8. *In vitro* cytotoxicity assessment and cellular uptake and internalization

Cytotoxicity was determined following an MTT assay.[38] Briefly, following 24 h seeding of MDA-MB-231 cells at a predetermined concentration (10^4 cells per well) in 96 well plates, the cells were treated with varying concentrations of AgNPs, pure QRC, QRC-AgNPs and QRC-FA-AgNPs. Following 48 h of incubation further incubation of the cells was carried out for 2 h with 0.5 mg ml^{-1} of MTT solution at 37 °C. Then, the medium consisting of MTT was aspirated with successive addition of DMSO (200 μl) in each well, ensuring solubilization of the formazan product thus formed. A microplate reader was used to measure the absorbance (Abs) at 570 nm and the comparative inhibition was calculated using:

$$(\text{Abs}_{\text{Control}} - \text{Abs}_{\text{treatment}})/\text{Abs}_{\text{Control}} \times 100\%.$$

The cellular uptake of the formulated AgNPs was evaluated in the MDA-MB-231 cells.[24] Briefly, the cells were seeded at a density of 5×10^4 cells in each well in 24 well plates, followed by 3 h incubation with fluorescein isothiocyanate (FITC) labeled AgNP and QRC-FA-AgNPs. For FITC labelling, 100 mg fabricated AgNPs were added to 1 ml of FITC solution in absolute alcohol. Then, centrifugation of this mixture after 4 h was consecutively

followed by vacuum drying to obtain FITC-AgNP and FITC-QRC-FA-AgNP. A folic acid competition assay was performed by co-incubating the QRC-FA-AgNPs with FA. Then, the cells were washed thrice with PBS and subjected to fixation in para-formaldehyde solution (4%) with successive staining with Hoechst 33 342 solution (10 μg ml^{-1}) in the dark for an hour. Finally, the fluorescence of cells was analyzed using a confocal microscope (FLOWVIEW, Olympus).

2.9. Annexin V staining and flow cytometry to analyze apoptosis[38]

MDA-MB-231 cells at a density of 2×10^6 cells were subjected to treatment with AgNPs, pure QRC, QRC-AgNPs, QRC-FA-AgNPs and QRC-FA-AgNPs + NIR at predetermined concentrations for 24 h. Consequently, the cells were tryptinized and harvested along with PBS washing and then resuspended in binding buffer (100 μl) comprising $CaCl_2$ (1 mM), $MgCl_2$ (0.75 mM), KCl (4 mM), NaCl (140 mM) and 4-(2-hydroxyethyl)piperazine-1-ethanesulfonic acid (HEPES) (10 mM) in double-distilled water (DDW). This was followed by 30 min staining of the suspended cells with annexin V-alexa fluor 647 (BD Biosciences, San Diego, USA) at 4 °C and the addition of propidium iodide (PI) to the stained cells after proper washing. Immediately after this, the cells were analyzed using a BD FACS calibur Flow Cytometry System and FCS Express software (BD Bioscience, USA) was used for evaluating the results.

2.10. Analysis of *in vitro* photo-chemothermal efficacy[24]

Determination of the photothermal effect on MDA-MB-231 cells was performed by incubating the cells with appropriate concentrations of AgNPs, QRC-AgNP and QRC-FA-AgNPs for 3 h followed by laser irradiation (800 nm, 1.5 W cm^{-2}, 5 min). Following an additional incubation for 3 h the cells were first washed carefully with subsequent staining with calcein-acetoxymethyl (AM) and PI as per the manufacturer's instructions (Cell health assay kit, Cell Signaling Technology). The chemo-photothermal effect was elucidated by incubating the cells with varying concentrations of AgNPs and QRC-FA-AgNPs for 3 h with subsequent exposure to NIR laser irradiation (800 nm, 1.5 W cm^{-2}) for 5 min. After a successive 24 h of incubation of the cells, an MTT assay was performed to assess the cell viability.

2.11. Intracellular ROS levels[39]

ROS production was estimated with the help of a dichlorodihydro-fluorescein diacetate (DCFH-DA) analysis kit (Abcam) following the manufacturer's guidelines. Briefly, MDA-MB-231 cells were primarily seeded in a 96 well plate. Treatment of cells with AgNPs, QRC-AgNPs, and QRC-FA-AgNPs was successively followed by removal of the media and further incubation of the cells with DCFH-DA (10 μM) and Hanks buffered salt solution (HBBS, 100 μl) for 30 min at 37 °C. Measurement of the ROS was carried out with a spectrofluorometer.

2.12. *In vivo* study design

The virgin female Sprague-Dawley (SD) rats (50–55 days old) required for the study were procured from the Central Animal Facility, Birla Institute of Technology (BIT) Mesra, Ranchi, Jharkhand, India (Reg. no. 1968/PO/Re/S/17/CPCSEA). The study was conducted in accordance with all the CPCSEA standards for the animal habitat, victuals and ethical considerations (Institutional Animals Ethics Committee, BIT Mesra, Ranchi, India) (1972/PH/BIT/61/18/1AEC).

Random distribution of the animals was performed meaning that six SD rats were included in each of the eight experimental groups. The complete *in vivo* study design of 118 d (ref. 40) is illustrated schematically in Fig. S1 (ESI).† The method for breast cancer induction in the SD rats, as well as the duration of the treatment with various drug formulations has been selected and performed following previously published studies.[41–46] Control rats in group I were administered with only the vehicle (olive oil (0.5 ml) on the day of induction and the treatment involved 1% sodium carboxymethyl cellulose (CDH, New Delhi, India)). Cancer was induced in SD rats belonging to group II (induced control) through the slightly modified air pouch technique[40] and they received 20 mg DMBA (suspended in 0.5 ml olive oil) on day 0. After 90 d of the tumor induction phase, the animals belonging to group III–VIII were treated with various drug formulations and/or laser for 28 d (ref. 41–46) and categorized as treatment groups. Group III animals received tail vein injections of AgNPs (40 mg kg^{-1}, body weight (b.w.)), group IV rats were given pure QRC (20 mg kg^{-1}, b.w., intravenously (i.v.)). Group V rats were exposed solely to NIR irradiation (800 nm, 1.5 W cm^{-2} for 5 min) for 14 d (every alternate day of the 28 d treatment protocol), and the group VI and VII animals received QRC-AgNPs and QRC-FA-AgNPs (equivalent to the amount of raw QRC administered, i.v.) respectively. Group VIII animals were treated for 28 d with QRC-FA-AgNPs (equivalent to the amount of raw QRC administered, i.v.) along with irradiation with continuous wave (c.w.) NIR laser (800 nm, 1.5 W cm^{-2} for 5 min) 24 h post-drug administration (*i.e.* 14 d, every alternate day for the 28 d treatment protocol). The entire experimental schedule included regular weekly monitoring of the b.w., as well as tumor location by palpation. After completion of the entire experimental protocol of 118 d, the animals were sacrificed and perfused with subsequent isolation of the mammary tissues and other vital organs (liver, lungs, kidneys, heart, brain and spleen). While sections of isolated breast tissues were either preserved for performing fluorescence terminal deoxynucleotidyl transferase deoxyuridine triphosphate nick end labeling (TUNEL) assay and field emission scanning electron microscope (FESEM) analysis, the vital organs tissues were processed for histopathological evaluations.

2.13. FESEM analysis of mammary tissues[47]

Mammary tissues isolated from all the animal groups were primarily fixed in buffered formalin (10% v/v) and then subjected to dehydration with increasing strength of ethanol (70% v/v ethanol for 3 h followed by 80%, 90% and 100% v/v for 1 h respectively). After drying the tissue samples using a critical

point dryer (CPD), they were mounted on stubs, sputter-coated with a gold layer and observed using FESEM (Sigma 300, ZEISS, Carl Zeiss).

2.14. *In vivo* apoptosis rate analysis through TUNEL assay[24]

The tumor tissues isolated from all the groups of animals were primarily subjected to paraffin block embedding prior to a TUNEL assay to verify intra-tumoral late stage apoptosis. Click iT plus TUNEL assay kit (Thermo-Fisher) which employs Alexa Fluor 594 for *in situ* detection of apoptosis was used for staining the tissue sections (30 μm) in accordance with the manufacturer's instructions. Successively, the stained tissues slices were observed using a confocal microscope (FLOWVIEW, Olympus).

2.15. Histopathological analysis[47]

Following sacrifice, vital organs such as the heart, lungs, liver, kidneys, spleen and brain were isolated from the study animals and embedded in paraffin wax, a rotary microtome was used to cut fine tissue sections (6–8 μm) of these paraffin blocks comprising tissue. Then, these tissue sections were stained with haematoxylin and eosin dye following the standard experimental protocol.

2.16. Statistical analysis

Statistical comparisons of the data were determined by using one-way analysis of variance (ANOVA), followed by Bonferroni's multiple comparison tests with a similar number of samples. The level of significance was measured at $p < 0.05$. All data were represented as mean ± standard error of the mean (SEM).

3. Results and discussion

One of the major problems with regards to chemotherapy is the dexterity of cancer cells to evade apoptosis, leading to therapy resistance. Thus, exploring key target molecules, as well as a stable delivery system, with a unique strategy to surpass resistance and restrict the side effects of the chemotherapeutic agents are the primary objectives of any ideal cancer therapy protocol.[48] However, various marketed drug delivery systems, such as those in trials are presently polyethylene glycol (PEG) based chemotherapeutic molecules. However, these are associated with issues relating to the balancing of the load with the holding capacity of the liposomal compartments with respect to the overall size of the nanoparticles, allowing uptake for intracellular localization.[49] Therefore, in this study we mainly aimed to synthesize FR-targeting plasmonic silver nanoparticles for QRC (QRC-FA-AgNPs) to investigate its cytotoxic and anti-apoptotic efficiency in combination with photothermal therapy.

3.1. UV-visible-NIR absorption spectra analysis of QRC-FA-AgNPs

The AgNPs synthesized at an optimum hydrazine concentration of 40 mM (5 °C and pH 5) manifested efficient plasmon tunable peaks from visible light to NIR. As shown in Fig. 1A, the first surface plasmon resonance peak (SPR1) was observed at 408 nm, characteristic of the silver nanoparticles with a second distinctly prominent peak (SPR2) at 800 nm. Following folic acid conjugation along with QRC quenching (Fig. 1B), the nanoparticles were observed to be optically active with a marked red shift of SPR2 (800 → 861 nm) showing a strong NIR individual resonance while SPR1 (408 → 472 nm) became less prominent. However, a considerable red shift in both surface plasmon resonance peaks (SPRs) indicated FA and QRC conjugation on the surface of the AgNPs.[24,50] On the other hand, absorption peaks for QRC-FA-AgNPs at 269 and 350 nm represented the successful conjugation and quenching of QRC and FA respectively, as these peaks corroborated with the absorption spectra of the physical mixture of QRC + FA (Fig. 1C) that showed characteristic peaks at 265 and 350 nm corresponding to raw QRC and raw FA, respectively.[51,52]

3.2. FT-IR analysis

The interactions and conjugation of FA and QRC was effectively studied using FT-IR spectroscopy. Fig. 1D demonstrates the peaks corresponding to the raw FA, QRC, the physical mixture of FA + QRC(R) along with the respective nanoparticles FA-AgNPs, QRC-AgNPs and QRC-FA-AgNPs. Raw QRC revealed the typical IR bands/peaks at 601.79, 682.80, 821.68 (characteristic of the out of the plane bending), 1168.86 (corresponding to the C–CO–C stretch and bend in ketones), 1199.72 (characteristic of the C–O stretch in phenols), 1265.30 (corresponding to the C–O stretching in the aryl ether ring), 1319.30 (in plane bending band of the C–H in the aromatic hydrocarbon), 1381.30, 1519.90, 1562.34, 1612.49 (characteristic of the aromatic ring stretch band), 1662.64 (correlating to the C═O aryl ketonic stretch), 3406.29, and 3321.06 cm^{-1} (corresponding to the OH stretching).[53] The characteristic peaks of FA at 1107.14 (owing to the C–O alcoholic stretch of pteridine ring), 1693.50 (C═O bond stretching vibration of the carbonyl group), 3119.82 and 3321.42 cm^{-1} (corresponding stretching vibration of N–H and O–H groups) were also clearly visible.[52] These identifying peaks for both QRC and FA were found in the infrared (IR) spectral pattern of their physical mixture, with minor broadening or shift of peaks. Moreover, the synthesized nanoparticles exhibited similar spectral patterns to that of the raw ingredients with certain alterations in the vibrational frequencies. This indicates the successful conjugation of FA and QRC on the anisotropic silver nanoparticles. The shift in the spectral peaks was observed in many cases after drug loading,[54] similar to our previous study, thus confirming the loading of the drug.

3.3. XRD analysis of the synthesized plasmonic nanoparticles

The XRD spectral pattern of the QRC loaded folate targeted nanoparticles was evaluated by comparison with that of the raw ingredients, as shown in Fig. 1E. QRC-FA-AgNP demonstrated characteristic diffraction peaks of AgNPs at 38.11° (111), 44.22° (200), 64.42°(220), and 77.48° (311), which were in accordance with previous studies,[52] along with identifying peaks of raw FA at 2θ values ranging from 20–30° (mainly at 22.65°, 27.08° and 29.49°).[55,56] The synthesized QRC loaded nanoparticles also

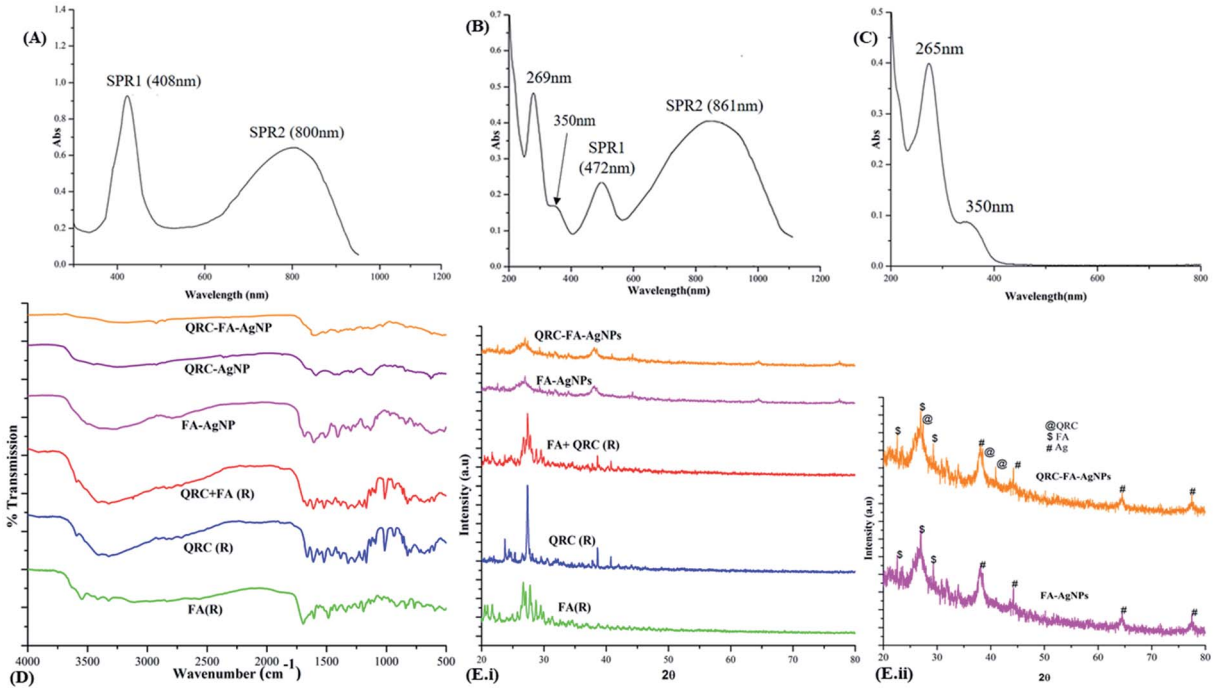

Fig. 1 Synthesis and characterization of QRC quenched FA modified plasmonic anisotropic silver nanoparticles (QRC-FA-AgNPs): (A) plasmon peaks of AgNPs (SPR1: 408 nm and SPR2: 800 nm) formulated in a single step chemical method; (B) characteristic absorption peak of QRC at 269 nm and FA at 350 nm with significant red shift of SPR1 and SPR2 denoting successful drug quenching and folic acid conjugation; (C) characteristic absorption peaks of QRC and FA in the physical mixture; (D) FT-IR spectra showing characteristic IR bands or peaks of FA (R), QRC (R), FA + QRC (physical mixture) (R), FA-AgNPs, QRC-AgNPs and QRC-FA-AgNPs; (E(i) and (ii)) XRD spectral pattern showing characteristic peaks of FA (R), QRC (R), FA + QRC (physical mixture) (R), FA-AgNPs, and QRC-FA-AgNPs.

showed peaks at 27.38°, 38.5° and 40.92° that corresponded to the XRD pattern of pure QRC,[57] as shown in Fig. 1E(i). Fig. 1E(ii) reveals a closer view of both the FA and QRC conjugated nanocrystals, which shows some broadening of the peaks with little noise, which has previously been reported to be imparted owing to surface modification or coating of nanoparticles.[58]

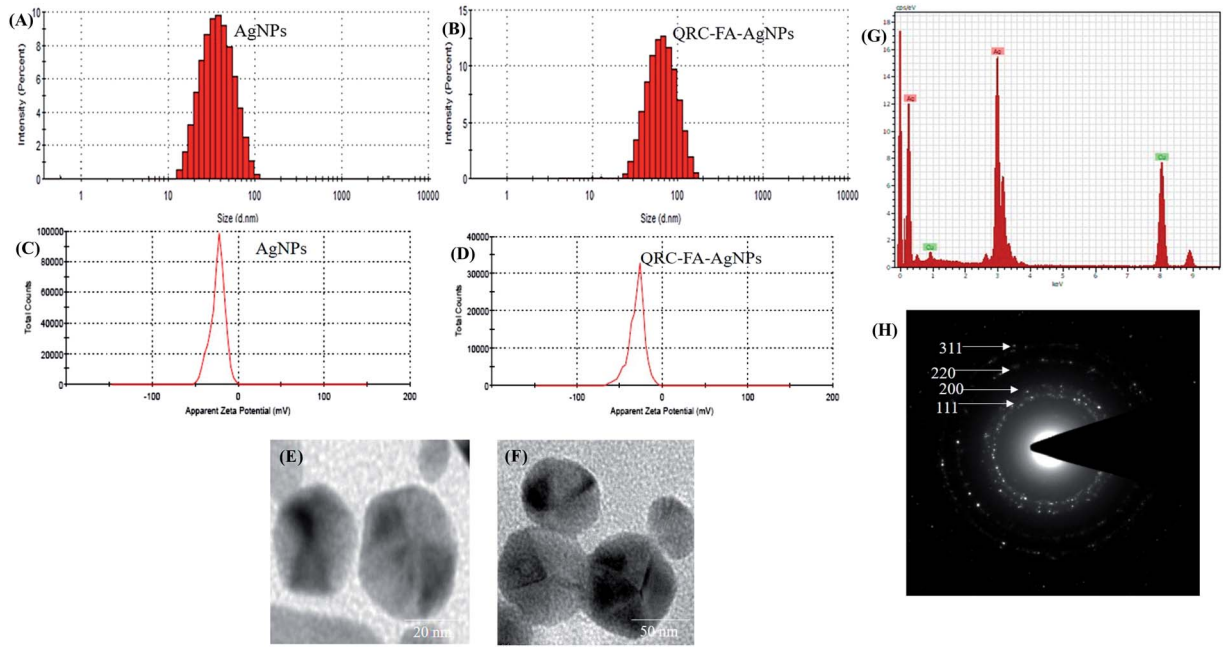

Fig. 2 Morphological analysis of silver nanoparticles: particle size distribution of: (A) AgNPs and (B) QRC-FA-AgNPs. Zeta potential of (C) AgNPs and (D) QRC-FA-AgNPs. High resolution TEM images of (E) AgNPs and (F) QRC-FA-AgNPs. (G) EDX analysis. (H) SAED analysis.

3.4. Hydrodynamic particle size and surface charge analysis along with morphological evaluation through TEM and EDX

As shown in Fig. 2A, the particle size of the plasmonic nanoparticles (blank AgNPs) were found to be 19.68 ± 0.58, while after FA conjugation, as well as QRC quenching, the particle size was found to be 47.58 ± 0.49 nm (Fig. 2B). High resolution (HR)-TEM revealed the shape of particles (blank and QRC-FA-AgNPs) to be distinctly pentagonal nanopyramids (Fig. 2E and F). These pentagonal QRC-FA-AgNPs demonstrated a robust plasmon tunability in the UV-vis-NIR region thus allowing absorption of light at higher wavelengths (~860 nm), which also facilitated deep tissue penetration. This phenomenon may result from plasmon coupling of adjoining nanoparticles as shown in previous studies.[59,60] The PDI values 0.246 ± 0.02 (AgNPs) and 0.265 ± 0.05 (QRC-FA-AgNPs) indicated a homogeneous and uniform dispersion of the nanoparticles (PDI < 3) which was also supported by the TEM images. Moreover, the zeta potential of the AgNPs (Fig. 2C) was found to be −24.0 mV, which may be imparted owing to the use of citrate as the capping agent.[25] Following the FA conjugation and QRC loading, the nanocarriers revealed a further negative surface charge of −33.5 mV (Fig. 2D) owing to folic acid functional groups and the negative OH groups of QRC.[25] Thus, while the overall particle size was well below 100 nm, the permitted feasibility for the cellular entry essential for drug delivery applications,[61] the negative zeta potential of QRC-FA-AgNPs resulted in repulsion between them, thus preventing flocculation and allowing stability of the formulation[62] with proper dispersity.

On the other hand, the EDX (Fig. 2G) performed using the TEM validated synthesized nanoparticles comprised elemental silver (Ag), as a distinct absorption peak at around 3 KeV was observed, which is an identifying feature of metallic silver ascribed SPR.[61,63] The crystallinity and diffraction peaks of the synthesized AgNPs observed in the XRD spectra indexed to the (111), (200), (220) and (311) planes of the face centered cubic crystal AgNP structure were revalidated using SAED (Fig. 2H).[52,64]

3.5. Drug loading and stability studies of QRC-FA-AgNPs

The loading efficiency of the synthesized silver nanoparticles was analyzed with a UV-vis spectrophotometer and theoretical drug loading capacity (DLC). With the theoretical DLC being set at 10 wt%, the synthesized AgNPs revealed a DLC of 8.13% that indicated successful loading of the drug.

The stability of the synthesized nanoparticles is a prerequisite parameter that should be determined. As observed from Fig. 3A(i), the particle size (hydrodynamic diameter), as well as the PDI (Fig. 3A(ii)) of the QRC-FA-AgNPs varied slightly within an acceptable limit over the incubation period of 14 d in all the three biologically relevant media of deionized water, cell culture medium and PBS, thus denoting the absence of particle aggregation.

3.6. Drug release study

Controlling the release pattern of the drug plays a vital role in improving the bioavailability of the fabricated QRC-FA-AgNPs.

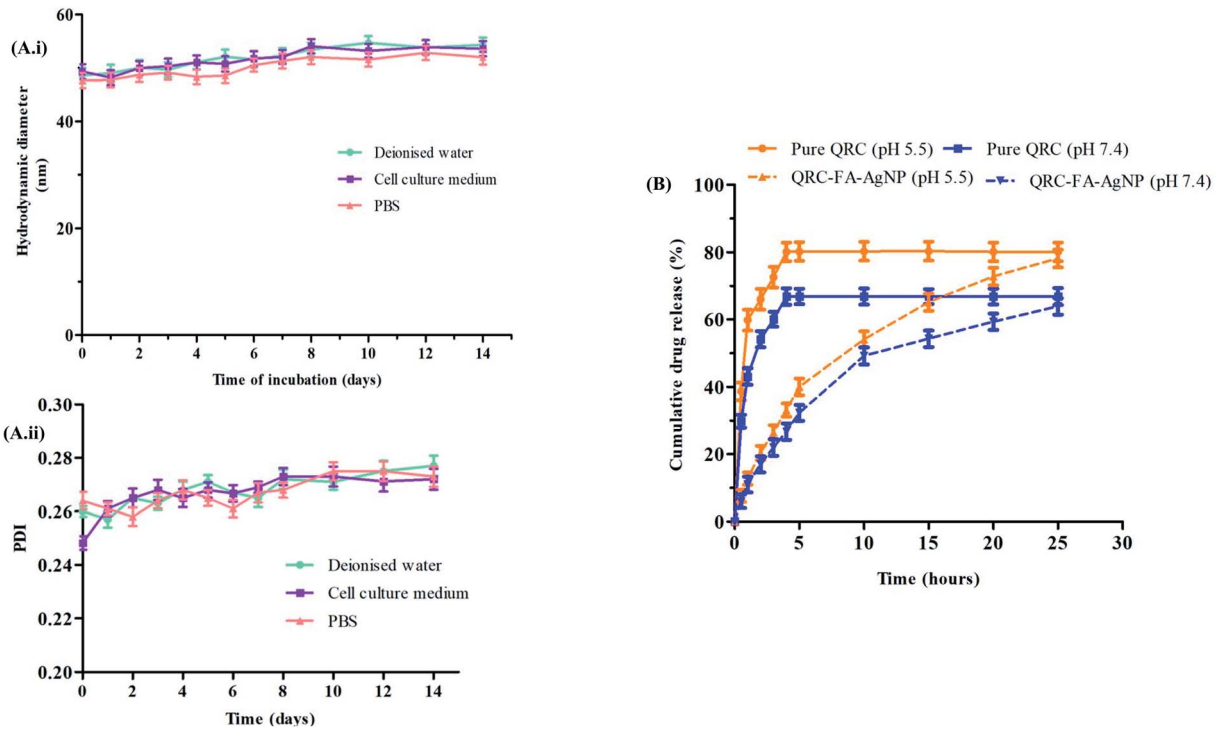

Fig. 3 (A) Stability of the synthesized QRC-FA-AgNPs in three biologically relevant media (deionized water, cell culture medium, and PBS) with respect to (i) hydrodynamic diameter and (ii) PDI. (B) The cumulative release study of QRC (R) at pH 5.5 and 7.4 respectively and QRC-FA-AgNPs at pH 5.5 and 7.4.

In this study, the release profile of QRC was evaluated from the QRC-FA-AgNPs at 37 °C in two buffered aqueous solutions, one with a pH of 5.5 mimicking the tumor microenvironment or intracellular endosomes and one with a pH of 7.4 similar to the physiological pH. The result revealed that the acidic condition stimulated a more rapid release of QRC from the NPs compared to the physiological neutral system. Fig. 3B demonstrates the release of 80.1% and 66.8% of free QRC within 4 h of the experimental period in buffer solutions of pH 5.5 and 7.4 respectively. However, in contrast to this, the QRC released from the QRC-FA-AgNPs was found to be only 33.13% and 26.71% at the corresponding pH over a period of 4 h. Thus, it was evident from the release curve that, although the release of the pure drug attained saturation within 5 h, QRC from the NPs leaked smoothly in less than 30 h at a variable pH status denoting the capability of the QRC-FA-AgNPs to specifically enhance the QRC delivery in cancer affected cells, correlating with earlier reports, which indicated that pH dependent drug release (*i.e.* increased efflux at acidic pH) significantly augments drug delivery to cancer cells as the tumor microenvironment is well known to be acidic.[61] Hence, the engineered plasmonic nanoparticles, having a sufficient loading efficiency and QRC release profile, may be considered as an optimal nanocarrier system for consolidated curative action.[65]

3.7. Improved targeted cellular internalization and *in vitro* cytotoxicity of QRC-FA-AgNPs

Folic acid fabricated nanocarriers have been diversely studied for therapeutic applications[66,67] as they provide a high selectivity to specific target folate receptors. The folate uptake mechanism is attributed to receptor mediated endocytosis, which involves initial internalization of a captured FA molecule by a FR followed by returning the FR to the cell surface for subsequent FA capture. A similar mechanism is applicable if FA is conjugated to nanoparticles.[24] Following internalization, the FA conjugates undergo dissociation in the acidic microenvironment of cancer cells and are released into cytosol.[68,69] In our study, the capability of specifically targeting folate receptors (FRs) present on breast cancer cells was investigated by the cellular internalization of FITC tagged QRC-FA-AgNPs in MDA-MB-231 cells. As shown in Fig. 4A, following the incubation of cells with QRC-FA-AgNPs, the green fluorescence intensity observed was much higher than that of cells incubated with bare AgNPs. Also, the overlay images of Hoechst + FITC + Phase demonstrated higher localization of the QRC-FA-AgNPs labelled with FITC in respect to AgNPs within the cells, indicating proper cellular internalization. This accentuated internalization may be a result of better recognition of FA functionalized AgNPs by FRs abundantly expressed on breast cancer cells, thus allowing adequate tumor specific accumulation of QRC-FA-AgNPs without harming the adjacent normal tissues. This observation was in accordance with previous studies involving diversified nanoscale carriers such as silver,[64] mesoporous silica, lignin based hollow nanoparticles,[70] Janus silver/silica based nanoplatforms[24] and so forth that revealed specific internalization and localization of nanoconjugates inside cellular organelles and the perinuclear region in each case. In order to confirm the FR targeted cellular uptake, co-incubation of cells with free folic

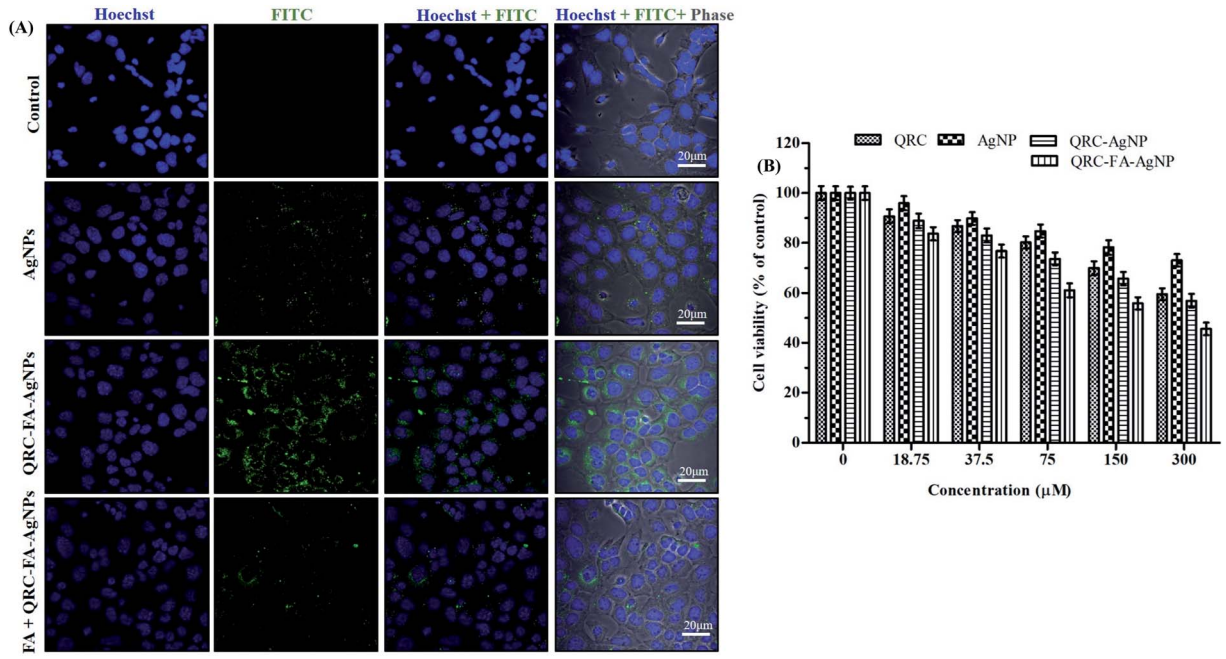

Fig. 4 Intracellular uptake and cell viability studies of QRC-FA-AgNPs. (A) CLSM images of MDA-MB-231 cells subjected to treatment with AgNPs, QRC-FA-AgNPs or free FA + QRC-FA-AgNPs. Blue fluorescence (Hoechst: dark blue) indicates cell nuclei location and the green fluorescence (FITC: green) denotes intracellular uptake and internalization of FITC-labelled QRC-FA-AgNPs. The scale bar represents 20 μm. (B) MTT assay for cell viability analysis following treatment of MDA-MB-231 cells with QRC, AgNPs QRC-AgNPs, and QRC-FA-AgNPs. The data are represented as mean ± SEM values.

acid was performed, which then indicated significant reduction in the green fluorescence of FA fabricated QRC-AgNPs, clearly suggesting that owing to competitive blockage of the FRs during FA pre-incubation resulted in diminished endocytosis of the nanoscopic-based cargoes.

3.8. Cytotoxic effects of QRC-FA-AgNPs as analyzed by MTT assay

As depicted in Fig. 4B, QRC-FA-AgNPs at different concentrations exhibited an escalating dose dependent toxicity in MDA-MB-231 cells. This elevated inhibitory rate of QRC-FA-AgNPs with respect to other formulations (blank AgNPs/QRC-AgNPs) or pure QRC on the viability of breast cancer cells may be explained as a consequence of the targeted cellular delivery and endocytosis of the nanocarriers *via* the FRs[71] making the cells more vulnerable to ROS and DNA damage. Consistent with our findings, former studies involving QRC loaded nanoparticles[61,72] had shown notable cytotoxicity towards MDA-MB-231, compared to pure QRC.

3.9. Apoptosis inducing potential of QRC-FA-AgNPs in MDA-MB-231 cells

Reactive oxygen species are also one of the principle regulators of mitochondria governed intrinsic apoptosis. QRC alone has already been reported to participate in initiating apoptosis in various cancer cell lines (*e.g.* HT29, CD33 + cancer stem cells, MCF-7, BCG-823)[73–75] while its nano-formulations (using gold/solid lipid nanoparticles) also effectively induce similar apoptotic mechanisms.[39,61] Additionally, AgNPs are known to bolster intrinsic apoptosis[65] attributed to ROS production, thereby activating proapoptotic factors in breast cancer or HepG2 cell lines.[58,76] Thus, to ensure that the chemotherapeutic potential of QRC-FA-AgNPs is mediated by apoptosis, fluorescence activated cell sorting (FACS) analysis was performed (Fig. 5A). As demonstrated in Fig. 5D, the QRC-AgNPs showed significantly high apoptosis with respect to pure QRC (Fig. 5C) or blank AgNPs (Fig. 5B). However, a remarkable upsurge in the early apoptosis indicated by AnnexinV+/PI− and late apoptosis as signified by annexin V+/PI+ breast cancer cells was observed following QRC-FA-AgNP treatment (Fig. 5E), which was further intensified by simultaneous laser exposure (Fig. 5F). Mediated by efficient folate targeting, the increased intracellular targeted uptake of QRC-FA-AgNPs resulted in a higher accumulation of the drug in cells and led to an enhanced apoptotic effect. Thus, plasmonic FA-AgNPs may act as an efficient carrier system for QRC for promoting the chemo-photothermal efficacy.

3.10. QRC-FA-AgNPs provoke prominent chemo-photothermal therapy

Recent pioneering studies focus on designing plasmonic nanoplatforms capable of exhibiting a strong NIR resonance in which negligible excitation light absorption and scattering is

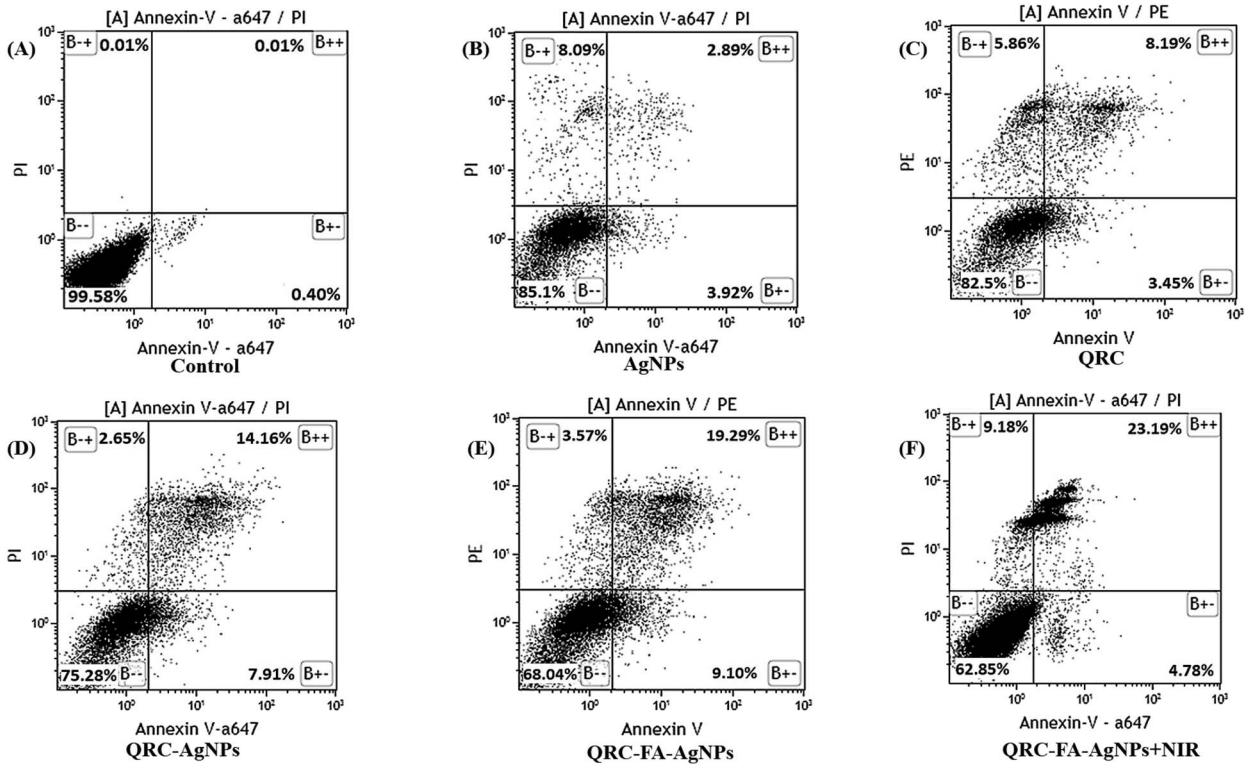

Fig. 5 Analysis of apoptotic cell death in MDA-MB-231 as documented by annexin V-alexa fluor 647(a647)/PI double staining and FACS analysis, in which: (A) control; (B) treated with AgNPs; (C) treated with pure QRC; (D) treated with QRC-AgNPs; (E) treated with QRC-FA-AgNPs; and (F) treated with QRC-FA-AgNPs + NIR. Apoptotic cells were annexin V [+] and PI [−], late apoptotic cells were annexin V [+] and PI [+], necrotic cells were annexin V [−] and PI [+] and the living cells annexin V [−] and PI [−].

exhibited by tissue chromophores (intrinsic) and water molecules enabling maximum tissue penetration of the radiation. Coupling of incident light with an oscillation frequency generated by conducting electrons of silver nanomaterials effectuate localized surface plasmon resonance (LSPR) that appears to be a strong absorbance band with a promising photo to heat transformation in tumor.[77] The proficiency of hyperthermia reaches a maximum if the wavelength of the laser coincides with the absorption maxima of NIR.[78] In this study, the photothermal effect of QRC-FA-AgNPs was thus intuitively analyzed by calcein-AM and PI staining that allowed live and dead cells to be distinguished following NIR laser irradiation. Fig. 6A exhibited no significant effect on the viability of cells when exposed solely to NIR irradiation. Cells incubated with AgNPs alone moderately increased the dead cell count after NIR exposure because of their ability to selectively heat the local environment as they convert light absorbed LSPR into heat which was further potentiated after QRC quenching. However, QRC-FA-AgNPs together with NIR showed the maximum dead cell count owing to higher internalization and accumulation of the nanocarriers inside cancer cells, facilitated by targeted endocytosis that improved the cytotoxicity of QRC along with production of sufficient local hyperthermia that enhanced the thermal sensitivity of breast cancer cells exposed to QRC. Similar results were observed in the cell viability study, in which the cells treated with QRC-FA-AgNPs exhibited maximum mortality under laser irradiation (Fig. 6A(ii)). Thus, the combined chemo-photothermal effect of the QRC-FA-AgNPs in the presence of NIR unveils an attractive strategy for improving the efficacy of QRC and balancing its dose.

Various researchers have reported promising cancer treatments (both *in vitro* and *in vivo*) induced by plasmonic nanoparticle triggered hyperthermia at the cellular, as well as the subcellular level.[79] It was evident from both our *in vitro* and successive *in vivo* assessments that upon exposure to NIR irradiation the QRC-FA-AgNPs provided an encouraging chemo-photothermal effect that improved the therapeutic efficacy in breast cancer. These findings were successfully correlated with the chemo-photothermal effect as reported in the case of Janus silver/silica nanoplatforms for the treatment of liver cancer,[24] FA-conjugated silver nanotriangles for human ovarian cancer cells[25] and human non-small lung cancer cells,[73] graphene oxide mediated synergistic chemo-photothermal effect on murine mammary cancer cell line.[80]

3.11. QRC-FA-AgNPs provokes intracellular ROS upsurge

The toxicological effect of the synthesized AgNPs is interlinked with their capability to provoke oxidative stress driven by intracellular ROS.[81] The tendency of AgNPs to localize in mitochondria collaborates with mitochondrial toxicity by increasing the ROS production.[76] In the current study, the ability of the

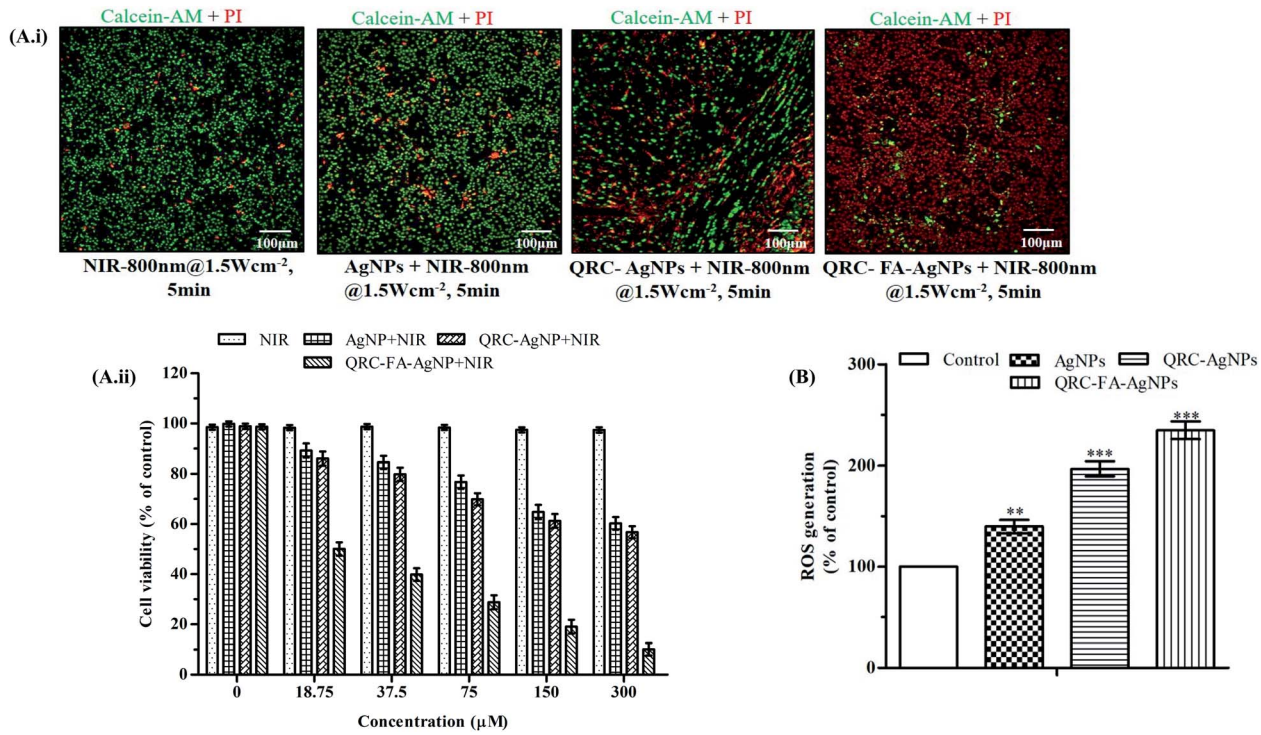

Fig. 6 (A) *In vitro* analysis of chemo-photothermal effect of QRC-FA-AgNPs: (i) fluorescence images of MDA-MB-231 cells treated with NIR (800 nm, 1.5 W cm^{-2}, 5 min), AgNPs + NIR (800 nm, 1.5 W cm^{-2}, 5 min), QRC-AgNP + NIR (800 nm, 1.5 W cm^{-2}, 5 min), QRC-FA-AgNPs + NIR (800 nm, 1.5 W cm^{-2}, 5 min) (green fluorescence: calcein-AM, red fluorescence: propidium iodide); (ii) cell viability analysis of MDA-MB-231 cells treated with NIR (800 nm, 1.5 W cm^{-2}, 5 min), AgNPs + NIR (800 nm, 1.5 W cm^{-2}, 5 min), QRC-AgNP + NIR (800 nm, 1.5 W cm^{-2}, 5 min) and QRC-FA-AgNPs + NIR (800 nm, 1.5 W cm^{-2}, 5 min), in which mean ± SEM values. (B) Estimation of ROS generation in the MDA-MB-231 cell line (DCF formation) following treatment with AgNPs, QRC-AgNPs, QRC-FA-AgNPs. Values are expressed as mean ± SEM, ($n = 3$). Comparison: ***$p < 0.001$; **$p < 0.01$; *$p < 0.05$; $^{ns}p > 0.05$ *versus* control.

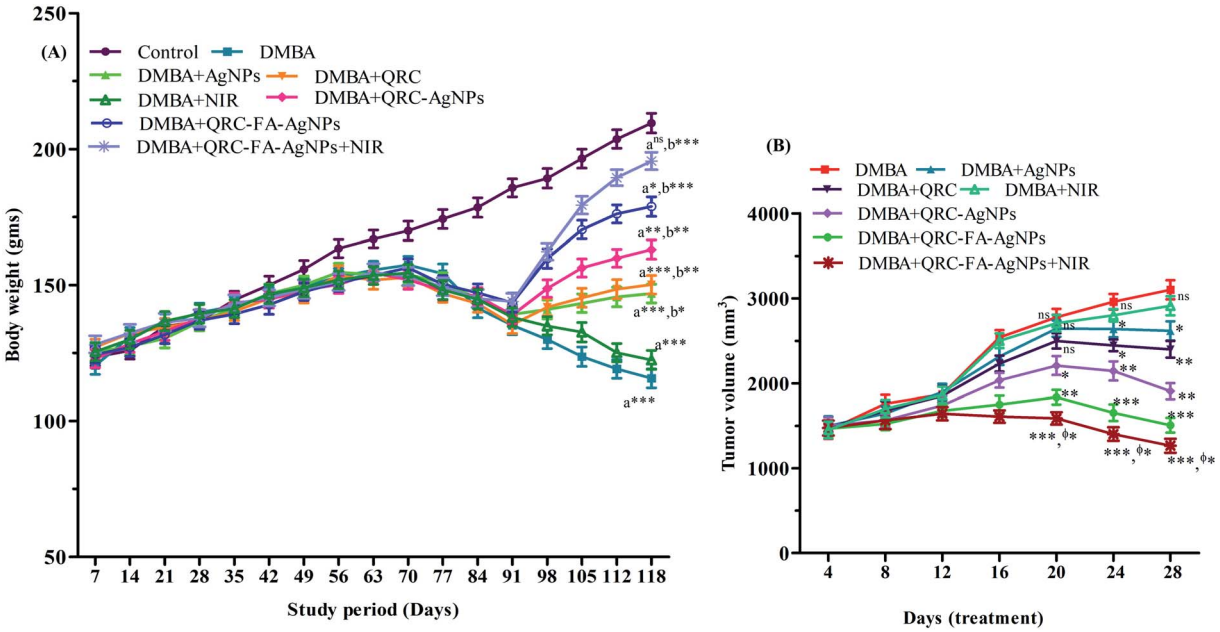

Fig. 7 *In vivo* analysis of combined chemo-photothermal effect of QRC-FA-AgNPs on (A) body weight, in which mean ± SEM ($n = 6$); comparisons: (A) group II, III, IV, V, VI, VII, VIII compared with group I; (B) group III, IV, V, VI, VII, VIII compared to group II; (B) tumor volume in cancer induced rats, in which mean ± SEM ($n = 6$); comparisons: group III, IV, V, VI, VII, VIII compared to group II each value shows ***$p < 0.001$; **$p < 0.01$; *$p < 0.05$; $^{ns}p > 0.05$; and ϕ-group VII compared with group VIII, each value shows *$p < 0.05$; $^{ns}p > 0.05$; group I – control; group II – induced control (DMBA, 20 mg); group III – DMBA (20 mg) + AgNP (40 mg kg^{-1}, b.w.); group IV – DMBA (20 mg) + QRC (20 mg kg^{-1}, b.w.); group V – DMBA (20 mg) + NIR (800 nm, 1.5 W cm$^{-2,}$ 5 min), group VI – DMBA (20 mg) + QRC-AgNP (20 mg kg^{-1}, b.w.); group VII – DMBA (20 mg) + QRC-FA-AgNP (20 mg kg^{-1}, b.w.), group VIII – DMBA (20 mg) + QRC-FA-AgNP (20 mg kg^{-1}, b.w.) + c.w. NIR (800 nm, 1.5 W cm$^{-2,}$ 5 min).

different formulated AgNPs for inducing intracellular ROS production was investigated using the green fluorescence stain DCFH-DA. As apparent from the results (Fig. 6B), QRC-AgNPs, as well as QRC-FA-AgNPs, were involved in significant accretion of ROS ($p < 0.001$) in MDA-MB-231 which corroborates the earlier investigations.[76]

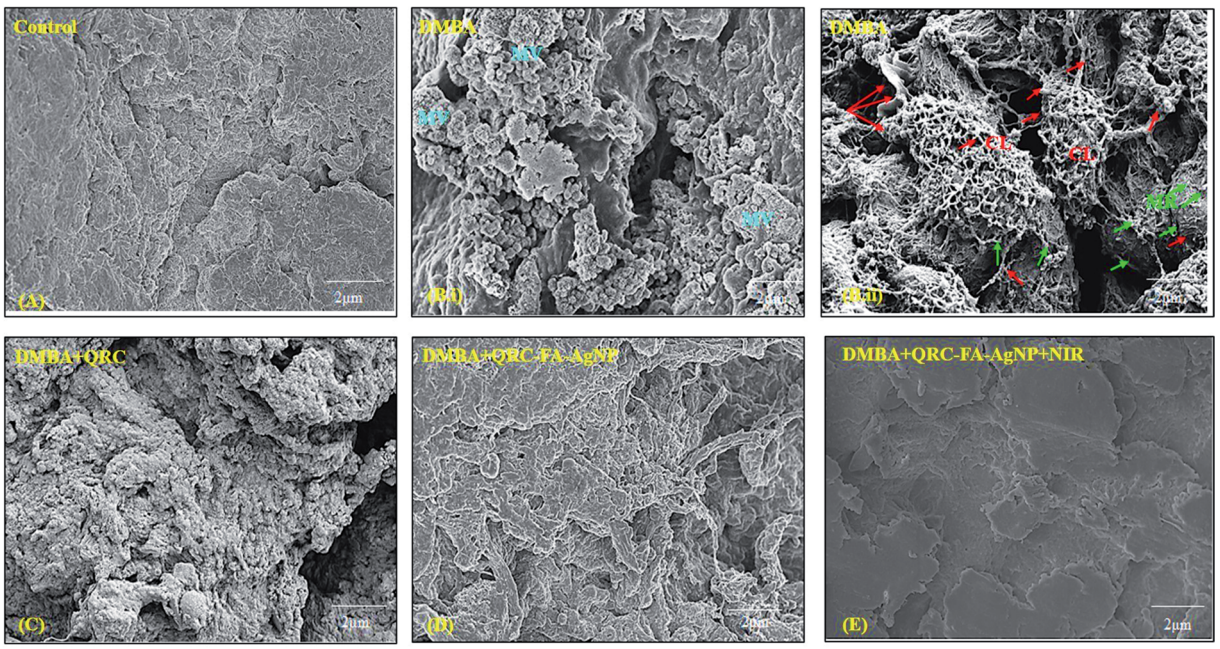

Fig. 8 Photomicrographic depiction of breast tissues isolated from different experimental groups of animals by FESEM to analyze the structural morphological alterations, in which (A) group I – control; (B(i) & (ii)) group II – induced control (DMBA, 20 mg); (C) group IV – DMBA (20 mg) + QRC (20 mg kg^{-1}, b.w.), (D) group VII – DMBA (20 mg) + QRC-FA-AgNP (20 mg kg^{-1}, b.w.), (E) group VIII – DMBA (20 mg) + QRC-FA-AgNP (20 mg kg^{-1}, b.w.) + c.w. NIR (800 nm, 1.5 W cm^{-2}, 5 min). The arrows have been color coded; red arrows indicate CL and green arrows indicate MR.

3.12. QRC-FA-AgNP remodeled DMBA-induced body weight changes and inhibited mammary tumorigenesis of breast cancer bearing animals

The weekly changes in body weight (b.w.) recorded for the entire study protocol (118 d) are illustrated in Fig. 7A. A gradual and normal increase in b.w. was evident in the group I animals. Although in the initial 6–7 weeks of the proliferation stage, the b.w. of the cancer induced animals in group II was found to increase gradually, the latter stage was marked with subsequent reduction in b.w. that was highly significant ($p < 0.001$) with reference to the group I animals at the end of the 118 d. Previous studies have also depicted a similar pattern of b.w. changes in cancer bearing animals, in which an accelerated decline in b.w. was observed from about 11 week following induction.[40,82] The anatomical variations, such as in b.w., reflect the abnormalities and physiological anomalies. The loss in body mass may be an outcome of cancer cachexia. Some of the distinguished symptoms of cachexia are reduced b.w., early satiety, as well as anorexia, a non-specific type of anemia, and prominent muscle weakness along with changed host-metabolism or malabsorption.[83] Deterioration of b.w. is associated with loss of fat as well as muscle mass. The reduction in muscle mass may be attributed to the aggravated amount of alanine originating from degrading muscles and utilizing gluconeogenesis.[84] However, upon various drug treatments the b.w. of cancer induced animals has been found to increase in previous studies that denote their antineoplastic efficacy.[40–43] In our study, during the treatment phase (day 91 day 118), the animals receiving drug quenched silver nanoparticles (group VI, VII, VIII) also showed better improvements in the b.w. than those receiving blank AgNPs, raw QRC or NIR in comparison to the induced control group. QRC-FA-AgNPs (group VII) showed a highly significant increase ($p < 0.001$) in the b.w. of the cancer induced animals in comparison to the induced control group, which may be due to the targeted delivery of QRC achieved by the silver nanoparticles. Moreover, animals receiving laser irradiation in association with the administered QRC-FA-AgNPs (group VIII) successfully normalized the altered b.w. resulting in an almost insignificant ($p > 0.05$) difference with the control group animals (group I). Thus, animals receiving plasmonic drug quenched folate targeted AgNPs demonstrated maximum protection, indicating the potentiation of QRC efficacy achieved by the silver nanoplatform owing to the combined chemo-photothermal effect.

Administration of DMBA consistently results in progressive tumor development. Following induction with DMBA, cancer bearing SD rats attain promotion phase tumors after 90 d. In the multistage tumorigenesis process the promotional stage is regarded as the reversible phase and is commonly studied for evaluation of the therapeutic effect of any drug. Thus, the post 90 d phase in the DMBA induced breast cancer model is suitable for any anticarcinogenic drug to cause prevention, reversal or even slowing down of the carcinogenic process.[46,85] In the current study, we also administered drugs and/or a laser during this stage (*i.e.* 91–118 d) of our 118 d experimental protocol and the effect of the combined chemo-photothermal therapy during this 28 d treatment period[41–46] is depicted in Fig. 7B. Following cancer induction, animals in group II developed large sized

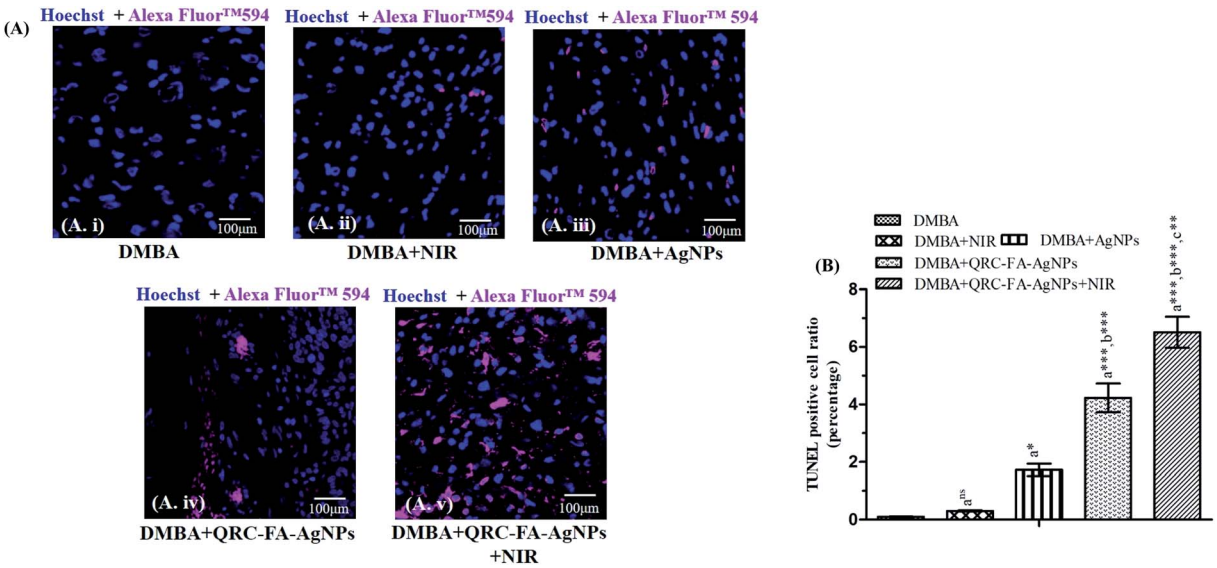

Fig. 9 TUNEL assay for *in vivo* apoptosis analysis: (A) representative TUNEL fluorescent images of section of tumor excised from rats of individual groups. Blue fluorescence (Hoechst: dark blue) indicates cell nuclei location and the purple fluorescence (Alexa Flour 594: purple) denotes apoptotic cell location. The scale bars are represented as 100 μm. (B) Estimation of rate of tumor apoptosis in rats belonging to each group in accordance to images of TUNEL assay in which each value shows mean ± SEM ($n = 6$); comparisons: (A) group III, V, VII, VIII compared with group II; (B) group VII, VIII compared to group III; (C) group VII compared with group VIII; ***$p < 0.001$; **$p < 0.01$; *$p < 0.05$; $^{ns}p > 0.05$; group II – induced control (DMBA, 20 mg); group III – DMBA (20 mg) + AgNP (40 mg kg^{-1}, b.w.); group V – DMBA (20 mg) + NIR (800 nm, 1.5 W cm^{-2}, 5 min), group VII – DMBA (20 mg) + QRC-FA-AgNP (20 mg kg^{-1}, b.w.), group VIII – DMBA (20 mg) + QRC-FA-AgNP (20 mg kg^{-1}, b.w.) + c.w. NIR (800 nm, 1.5 W cm^{-2}, 5 min).

tumors which were significantly reduced ($p < 0.001$) following QRC-FA-AgNP treatment (group VII) in comparison to pure QRC at the same dose as revealed by group IV animals (Fig. 7B). Moreover, when compared to group II animals, specific cancer cell ablation owing to hyperthermia achieved in rats belonging to group VIII by laser irradiation further improved the chemo-photothermal efficacy of QRC-FA-AgNPs in group VIII, thereby assisting in the targeted damage of tumor cells. Therefore, at the end of the 28 d treatment phase, the combined chemo-photothermal therapy revealed its potency to restrict and reduce tumor development.

Thus, the enhanced efficacy of QRC-FA-AgNPs to induce apoptosis was predominantly reflected by the b.w. and tumor volume of the breast cancer bearing animals that were successfully ameliorated upon treatment. However, the chemotherapeutic potential of QRC-FA-AgNPs was improved when the animals were exposed to NIR radiation that conferred maximum protection attenuating the tumor volume and reinstating b.w.

3.13. QRC-FA-AgNPs remodeled normal architecture in breast cancer tissues as illustrated by FESEM

In order to analyze the morphological changes in breast tumor tissues before and after treatment, FESEM was performed. As exhibited by Fig. 8B(ii), the breast cancer induced tissue showed membrane ruffles (MR) that indicate the invasiveness of the breast cancer and were also found to be densely covered with microvilli (MV) (Fig. 8B(ii)) that were absent in the control animal breast tissue (Fig. 8A). In addition, collagen fibers originating in the surrounding matrix were observed to crosslink and form a dense network with strings of protrusions emerging from cancer cells. However, the dense accumulation of collagen fibers (CL) including the network with the surrounding matrix was found to decrease remarkably following QRC-FA-AgNP therapy (Fig. 8D) in comparison to QRC treatment (Fig. 8C) and disappeared after irradiation to NIR subsequent to QRC-FA-AgNP treatment (Fig. 8E). The MR were also minimized with restoration of normal architecture of the breast tissue, which further validated the chemo-photothermal therapy to be one of the most effective therapeutic strategies in treating breast cancer.

3.14. Hyperthermia enhanced QRC-FA-AgNPs invoked *in vivo* apoptosis and tumor growth inhibition

A TUNEL assay was performed on the tumors excised from experimental animals and the rates of apoptosis were enumerated for further exploiting the mechanism associated with the combined antitumor activity. In Fig. 9A and B minimal fluorescence signals were visible in the DMBA treated and DMBA + NIR receiving animals. While animals receiving blank AgNPs showed signs of initiation of apoptosis. Cancer induced animals treated with QRC-FA-AgNPs revealed significantly advanced apoptosis. As manifested from our previous *in vitro* results, treatment with QRC-FA-AgNPs + NIR conferred a maximum rate of *in vivo* tumor apoptosis in comparison with the other groups of animals. Thus, the extent of intra-tumoral

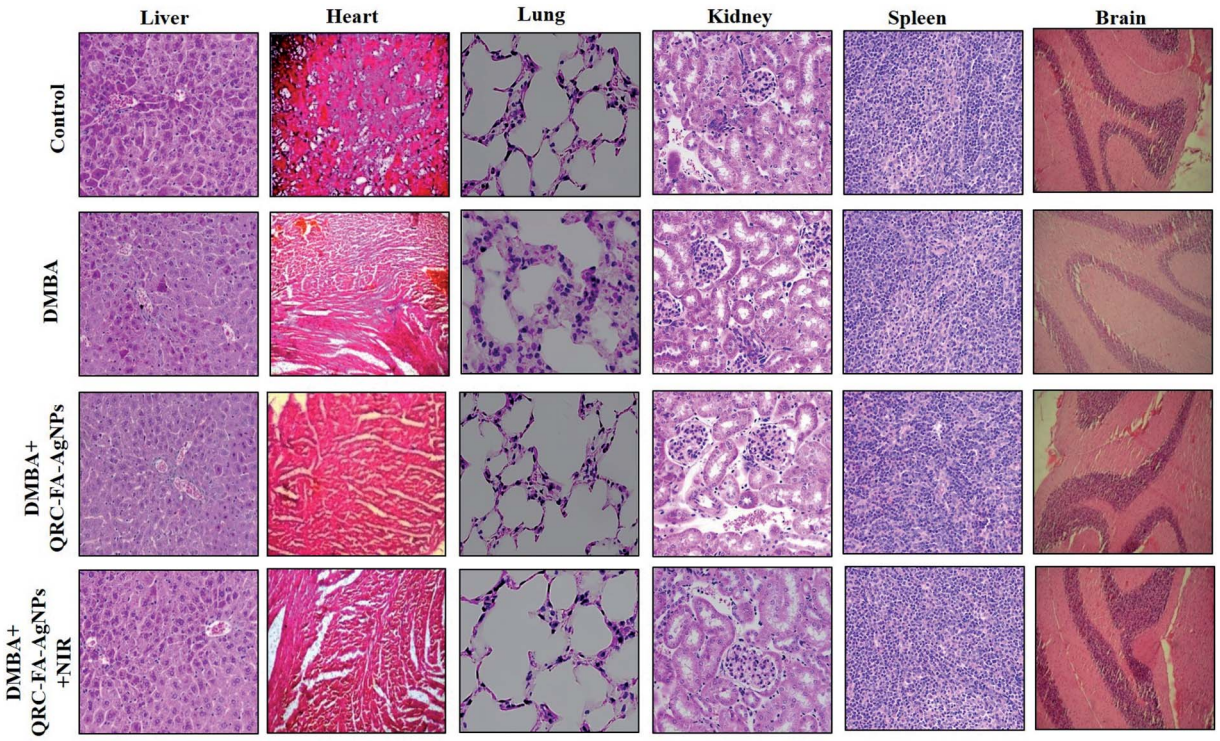

Fig. 10 Histopathological studies (H&E) staining of vital organs (lungs, liver, kidneys, heart, brain, and spleen) tissues to determine biocompatibility isolated from animals belonging to different experimental groups (400×) in which group I: control; group II – induced control (DMBA, 20 mg); group VII – DMBA (20 mg) + QRC-FA-AgNP (20 mg kg^{-1}, b.w.), group VIII – DMBA (20 mg) + QRC-FA-AgNP (20 mg kg^{-1}, b.w.) + c.w. NIR (800 nm, 1.5 W cm^{-2}, 5 min).

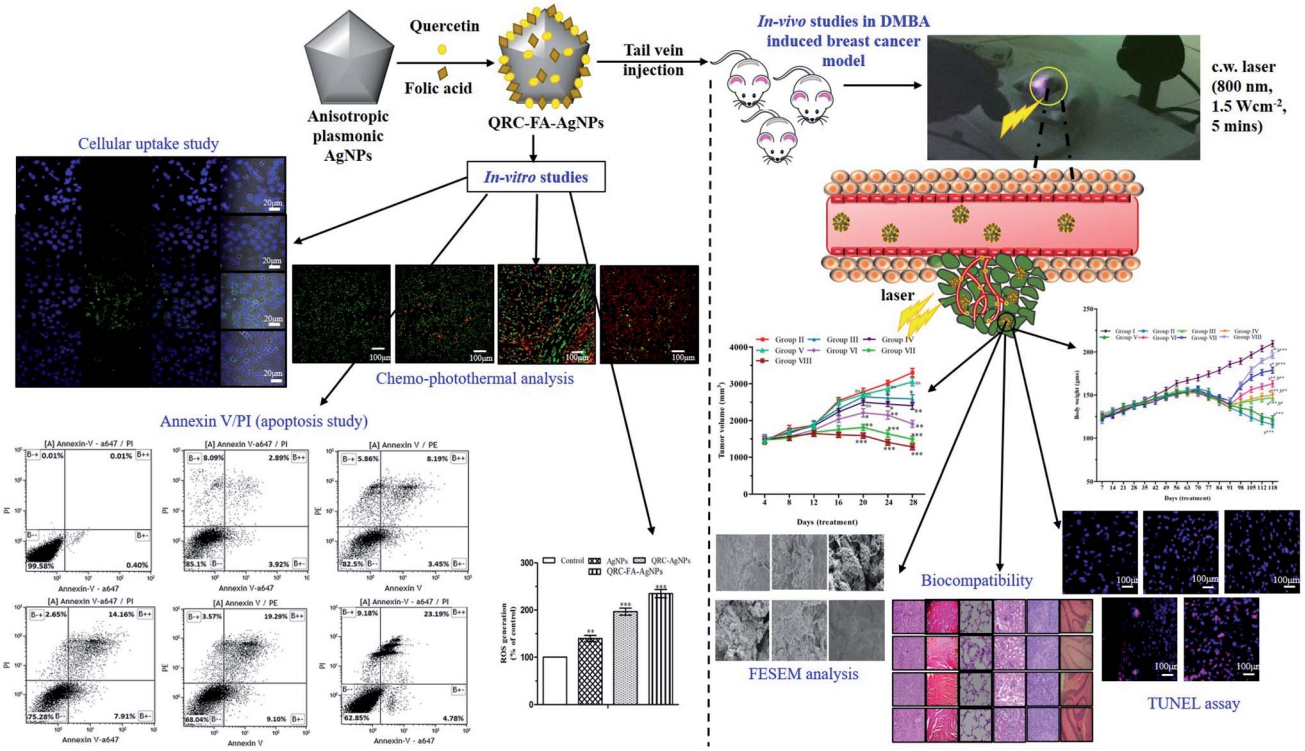

Fig. 11 *In vitro* and *in vivo* efficacy of light-activated combined chemo-photothermal therapeutic approach using QRC-FA-AgNPs for treatment of breast cancer.

apoptosis and TUNEL positive cells, respectively, clearly suggested the successful and improved tumor growth inhibition by the photothermal effect supplemented chemotherapeutic potency of QRC-FA-AgNPs in the presence of NIR.[24]

3.15. Biocompatibility of QRC-FA-AgNPs indicated by histopathological evaluation

Haematoxylin and eosin staining illustrated non-significant pathological alterations in the isolated vital organ tissues of the heart, liver, lungs, kidneys, brain and spleen indicating the absence of inflammation, lesions or tissue damage (Fig. 10). Animals belonging to groups VII and VIII showed an improved biocompatibility, organ specificity and targeted drug delivery owing to FA fabrication of the QRC loaded AgNPs when compared with animals receiving bare AgNPs and raw QRC, which showed subtle signs of acute inflammation in the vital organs, signifying signs of side effects that may be associated with free drug administration. Overall, QRC-FA-AgNPs serves as a biocompatible nano-delivery cargo for QRC, the efficacy of which can be improved when exposed to NIR irradiation mediated by photothermal therapy.

4. Conclusion

In contrast to the typical (spherical) AgNPs with a restrained plasmonic resonance at ~450–500 nm, a novel folate receptor targeted silver based QRC nano delivery system with characteristic plasmon tunability in the NIR region (~860 nm) was modelled in the current study for combined chemo-photothermal therapy of breast cancer. To surmount the inadequate water solubility of QRC and improve the biocompatibility, we designed favorable NIR triggered nano-cargoes that showed efficient internalization in breast cancer cells through folate receptors. Predominantly, the photothermal effect induced by the silver nanocarrier supplemented the antitumor efficacy of QRC by inducing hyperthermia, thus selectively killing the cancer cells and resulting in apoptosis. Moreover, the QRC loaded AgNPs exhibited a synergistic antitumor effect in both *in vitro* and *in vivo* investigations (Fig. 11). Conclusively, the functionally upgraded plasmonic QRC-FA-AgNPs proved to be more potent than free QRC and could be used as a sequential strategy for combined therapy for breast cancer.

Conflicts of interest

There are no conflicts to declare.

Financial support and sponsorship

This research was fully funded by AICTE under the project grant no. 8-69/RIFD/RPS/POLICY-1/2016-17.

Acknowledgements

The authors are immensely thankful to the BIT for offering all the necessary facilities and infrastructure for uninterrupted conduct of this work. The authors also greatly acknowledge

Central Instrumentation Facility (CIF, BIT, Mesra) for their uninterrupted assistance in the physico-chemical characterization of nanoparticles and HR-TEM facility of Vellore Institute of Technology.

References

1 American Cancer Society, *Breast Cancer Facts & Figures 2019–2020*, American Cancer Society, Atlanta, 2019.
2 M. Wang, J. Li, X. Li, H. Mu, X. Zhang, Y. Shi, Y. Chu, A. Wang, Z. Wu and K. Sun, Magnetically and pH dual responsive dendrosomes for tumor accumulation enhanced folate-targeted hybrid drug delivery, *J. Controlled Release*, 2016, **232**, 161–174.
3 Y. Xu, S. Asghar, H. Li, M. Chen, Z. Su, Y. Xu, Q. Ping and Y. Xiao, Preparation of a paclitaxel-loaded cationic nanoemulsome and its biodistribution via direct intratumoral injection, *Colloids Surf., B*, 2016, **142**, 81–88.
4 R. Abou-Jawde, T. Choueiri, C. Alemany and T. Mekhail, An overview of targeted treatments in cancer, *Clin. Ther.*, 2003, **25**, 2121–2137.
5 M. Saad, O. B. Garbuzenko and T. Minko, Co-delivery of siRNA and an anticancer drug for treatment of multidrug-resistant cancer, *Nanomedicine*, 2008, **3**, 761–776.
6 J. Vega, S. Ke, Z. Fan, S. Wallace, C. Charsangavej and C. Li, Targeting doxorubicin toepidermal growth factor receptors by site-specific conjugation of C225 to poly(L-glutamic acid) through a polyethylene glycol spacer, *Pharm. Res.*, 2003, **20**, 826–832.
7 I. J. Majoros, A. Myc, T. Thomas, C. B. Mehta and J. R. Baker, PAMAM dendrimer-based multifunctional conjugate for cancer therapy: Synthesis, characterization, and functionality, *Biomacromolecules*, 2006, **7**, 572–579.
8 J. Overgaard, Combined adriamycin and hyperthermia treatment of a murine mammary carcinoma *in vivo*, *Cancer Res.*, 1976, **36**, 3077–3081.
9 Y. Tang and A. J. McGoron, Combined effects of laser-ICG photothermotherapy and doxorubicin chemotherapy on ovarian cancer cells, *J. Photochem. Photobiol., B*, 2009, **97**, 138–144.
10 S. Srivastava, R. R. Somasagara, M. Hegde, M. Nishana, S. K. Tadi, M. Srivastava, B. Choudhary and S. C. Raghavan, Quercetin, a natural flavonoid interacts with DNA, arrests cell cycle and causes tumor regression by activating mitochondrial pathway of apoptosis, *Sci. Rep.*, 2016, **6**, 24049.
11 R. Tummala, W. Lou, A. C. Gao and N. Nadiminty, Quercetin targets hnRNPA1 to overcome enzalutamide resistance in prostate cancer cells, *Mol. Cancer Ther.*, 2017, **16**, 2770–2779.
12 D. W. Lamson and M. S. Brignall, Antioxidants and cancer, Part 3: Quercetin, *Alternative Med. Rev.*, 2000, **5**, 196–208.
13 A. Sarkar, S. Ghosh, S. Chowdhury, B. Pandey and P. C. Sil, Targeted delivery of quercetin loaded mesoporous silica nanoparticles to the breast cancer cells, *Biochim. Biophys. Acta, Gen. Subj.*, 2016, **1860**, 2065–2075.
14 P. J. Mulholland, D. R. Ferry, D. Anderson, S. A. Hussain, A. M. Young, J. E. Cook, E. Hodgkin, L. W. Seymour and D. J. Kerr, Pre-clinical and clinical study of QC12, a water-soluble, pro-drug of quercetin, *Ann. Oncol.*, 2001, **12**, 245–248.
15 S. S. Dhumale, B. N. Waghela and C. Pathak, Quercetin protects necrotic insult and promotes apoptosis by attenuating the expression of RAGE and its ligand HMGB1 in human breast adenocarcinoma cells, *IUBMB Life*, 2015, **67**, 361–373.
16 A. Rauf, M. Imran, I. A. Khan, M. ur-Rehman, S. A. Gilani, Z. Mehmood and M. S. Mubarak, Anticancer potential of quercetin: A comprehensive review, *Phytother. Res.*, 2018, **32**, 2109–2130.
17 J. Xie, S. Lee and X. Chen, Nanoparticle-based theranostic agents, *Adv. Drug Delivery Rev.*, 2010, **62**, 1064–1079.
18 W. Cai, T. Gao, H. Hong and J. Sun, Applications of gold nanoparticles in cancer nanotechnology, *Nanotechnol., Sci. Appl.*, 2008, **1**, 17.
19 S. Pattanayak, A. Swarnkar, A. Priyam and G. M. Bhalerao, Citrate–hydrazine hydrogen-bonding driven single-step synthesis of tunable near-IR plasmonic anisotropic silver nanocrystals: implications for SERS spectroscopy of inorganic oxoanions, *Dalton Trans.*, 2014, **43**, 11826–11833.
20 L. Wei, J. Lu, H. Xu, A. Patel, Z. S. Chen and G. Chen, Silver nanoparticles: synthesis, properties, and therapeutic applications, *Drug Discovery Today*, 2015, **20**, 595–601.
21 J. Liu, Y. Zhao, Q. Guo, Z. Wang, H. Wang, Y. Yang and Y. Huang, TAT-modified nanosilver for combating multidrug-resistant cancer, *Biomaterials*, 2012, **33**, 6155–6161.
22 P. Chairuangkitti, S. Lawanprasert, S. Roytrakul, S. Aueviriyavit, D. Phummiratch, K. Kulthong, P. Chanvorachote and R. Maniratanachote, Silver nanoparticles induce toxicity in A549 cells via ROS-dependent and ROS-independent pathways, *Toxicol. In Vitro*, 2013, **27**, 330–338.
23 S. Kittler, C. Greulich, J. Diendorf, M. Koller and M. Epple, Toxicity of silver nanoparticles increases during storage because of slow dissolution under release of silver ions, *Chem. Mater.*, 2010, **22**, 4548–4554.
24 Z. Wang, Z. Chang, M. Lu, D. Shao, J. Yue, D. Yang, M. Li and W. F. Dong, Janus silver/silica nanoplatforms for light-activated liver cancer chemo/photothermal therapy, *ACS Appl. Mater. Interfaces*, 2017, **9**, 30306–30317.
25 S. Boca-Farcau, M. Potara, T. Simon, A. Juhem, P. Baldeck and S. Astilean, Folic acid-conjugated, SERS-labeled silver nanotriangles for multimodal detection and targeted photothermal treatment on human ovarian cancer cells, *Mol. Pharm.*, 2014, **11**, 391–399.
26 W. S. Kuo, C. N. Chang, Y. T. Chang, M. H. Yang, Y. H. Chien, S. J. Chen and C. S. Yeh, Gold nanorods in photodynamic therapy, as hyperthermia agents, and in near-infrared optical imaging, *Angew. Chem., Int. Ed.*, 2010, **49**, 2711–2715.
27 X. Huang, I. H. El-Sayed, W. Qian and M. A. El-Sayed, Cancer cell imaging and photothermal therapy in the near-infrared region by using gold nanorods, *J. Am. Chem. Soc.*, 2006, **128**, 2115–2120.

28 R. S. Riley and E. S. Day, Gold nanoparticle-mediated photothermal therapy: applications and opportunities for multimodal cancer treatment, *Wiley Interdiscip. Rev.: Nanomed. Nanobiotechnol.*, 2017, **9**, e1449.

29 V. Agarwal and K. Chatterjee, Recent advances in the field of transition metal dichalcogenides for biomedical applications, *Nanoscale*, 2018, **10**, 16365–16397.

30 V. Agarwal, N. Varghese, S. Dasgupta, A. K. Sood and K. Chatterjee, Engineering a 3D MoS2 foam using keratin exfoliated nanosheets, *Chem. Eng. J.*, 2019, **374**, 254–262.

31 A. Pradhan, A. Kumari, R. Srivastava and D. Panda, Quercetin encapsulated biodegradable plasmonic nanoparticles for photothermal therapy of hepatocellular carcinoma cells, *ACS Appl. Bio Mater.*, 2019, **2**, 5727–5738.

32 S. Roy, A. Sarkar and A. Jaiswal, Poly (allylamine hydrochloride)-functionalized reduced graphene oxide for synergistic chemo-photothermal therapy, *Nanomedicine*, 2019, **14**, 255–274.

33 C. Murugan, N. Murugan, A. K. Sundramoorthy and A. Sundaramurthy, Nanoceria decorated flower-like molybdenum sulphide nanoflakes: an efficient nanozyme for tumour selective ROS generation and photo thermal therapy, *Chem. Commun.*, 2019, **55**, 8017–8020.

34 Z. Zhang, J. Wang, D. E. Tacha, P. Li, R. E. Bremer, H. Chen, B. Wei, X. Xiao, J. Da, K. Skinner and D. G. Hicks, Folate receptor α associated with triple-negative breast cancer and poor prognosis, *Arch. Pathol. Lab. Med.*, 2014, **138**, 890–895.

35 N. Currier, S. E. Solomon, E. G. Demicco, D. L. Chang, M. Farago, H. Ying, I. Dominguez, G. E. Sonenshein, R. D. Cardiff, Z. X. Xiao and D. H. Sherr, Oncogenic signaling pathways activated in DMBA-induced mouse mammary tumors, *Toxicol. Pathol.*, 2005, **33**, 726–737.

36 J. Buters, L. Quintanilla-Martinez, W. Schober, V. J. Soballa, J. Hintermair, T. Wolff, F. J. Gonzalez and H. Greim, CYP1B1 determines susceptibility to low doses of 7,12-dimethylbenz [a]anthracene-induced ovarian cancers in mice: Correlation of CYP1B1-mediated DNA adducts with carcinogenicity, *Carcinogenesis*, 2003, **24**, 327–334.

37 A. Priyam, N. Idris and Y. Zhang, Gold nanoshell coated NaYF4 nanoparticles for simultaneously enhanced upconversion fluorescence and darkfield imaging, *J. Mater. Chem.*, 2012, **22**, 960–965.

38 A. Kumar, P. Sunita, S. Jha and S. P. Pattanayak, Daphnetin inhibits TNF-α and VEGF-induced angiogenesis through inhibition of the IKK s/IκBα/NF-κB, Src/FAK/ERK 1/2 and Akt signalling pathways, *Clin. Exp. Pharmacol. Physiol.*, 2016, **43**, 939–950.

39 F. Niazvand, M. Orazizadeh, L. Khorsandi, M. Abbaspour, E. Mansouri and A. Khodadadi, Effects of quercetin-loaded nanoparticles on MCF-7 human breast cancer cells, *Medicina*, 2019, **55**, 114.

40 M. W. Haque, P. Bose, M. U. Siddique, P. Sunita, A. Lapenna and S. P. Pattanayak, Taxifolin binds with LXR (α & β) to attenuate DMBA-induced mammary carcinogenesis through mTOR/Maf-1/PTEN pathway, *Biomed. Pharmacother.*, 2018, **105**, 27–36.

41 M. W. Haque and S. P. Pattanayak, Taxifolin inhibits 7, 12-dimethylbenz (a) anthracene-induced breast carcinogenesis by regulating AhR/CYP1A1 signaling pathway, *Pharmacogn. Mag.*, 2017, **13**, S749.

42 P. Bose and S. P. Pattanayak, Herniarin, a natural coumarin, inhibits mammary carcinogenesis by modulating liver X receptor-α/β-PI3K-Akt-Maf1 Pathway in sprague-dawley rats, *Pharmacogn. Mag.*, 2019, **15**, 510.

43 A. Kumar, P. Sunita, S. Jha and S. P. Pattanayak, 7, 8-Dihydroxycoumarin exerts antitumor potential on DMBA-induced mammary carcinogenesis by inhibiting ERα, PR, EGFR, and IGF1R: involvement of MAPK1/2-JNK1/2-Akt pathway, *J. Physiol. Biochem.*, 2018, **74**, 223–234.

44 A. Kumar, S. Jha and S. P. Pattanayak, Daphnetin ameliorates 7, 12-dimethylbenz [a] anthracene-induced mammary carcinogenesis through Nrf-2-Keap1 and NF-κB pathways, *Biomed. Pharmacother.*, 2016, **82**, 439–448.

45 S. P. Pattanayak, P. Sunita and P. M. Mazumder, Restorative effect of Dendrophthoe falcata (Lf) Ettingsh on lipids, lipoproteins, and lipid-metabolizing enzymes in DMBA-induced mammary gland carcinogenesis in Wistar female rats, *Comp. Clin. Pathol.*, 2014, **23**, 1013–1022.

46 S. P. Pattanayak and P. M. Mazumder, Therapeutic potential of Dendrophthoe falcata (Lf) Ettingsh on 7, 12-dimethylbenz (a) anthracene-induced mammary tumorigenesis in female rats: effect on antioxidant system, lipid peroxidation, and hepatic marker enzymes, *Comp. Clin. Pathol.*, 2011, **20**, 381–392.

47 P. Bose, M. U. Siddique, R. Acharya, V. Jayaprakash, B. N. Sinha, A. Lapenna and S. P. Pattanayak, Quinazolinone derivative BNUA-3 ameliorated [NDEA+ 2-AAF]-induced liver carcinogenesis in SD rats by modulating AhR-CYP1B1-Nrf2-Keap1 pathway, *Clin. Exp. Pharmacol. Physiol.*, 2020, **47**, 143–157.

48 M. Ferrari, Cancer nanotechnology: opportunities and challenges, *Nat. Rev. Cancer*, 2005, **5**, 161–171.

49 T. M. Allen and P. R. Cullis, Drug delivery systems: Entering the mainstream, *Science*, 2004, **303**, 1818.

50 S. Sau, P. Agarwalla, S. Mukherjee, I. Bag, B. Sreedhar, M. Pal-Bhadra, C. R. Patra and R. Banerjee, Cancer cell-selective promoter recognition accompanies antitumor effect by glucocorticoid receptortargeted gold nanoparticle, *Nanoscale*, 2014, **6**, 6745–6754.

51 S. Sahu, S. Saraf and C. D. Kaur, Biocompatible nanoparticle for sustainable topical delivery of anticancer phytoconstituent quercetin, *Pak. J. Biol. Sci.*, 2013, **16**, 601–609.

52 B. K. Dadhich, B. Bhushan, A. Saha and A. Priyam, Folate-directed shape-transformative synthesis of hollow silver nanocubes: Plasmon tunability, growth kinetics, and catalytic applications, *ACS Appl. Nano Mater.*, 2018, **1**, 4294–4305.

53 M. Heneczkowski, M. Kopacz, D. Nowak and A. Kuzniar, Infrared spectrum analysis of some flavonoids, *Acta Pol. Pharm.*, 2001, **58**, 415–420.

54 D. Jeevitha and A. Kanchana, Evaluation of chitosan/poly (lactic acid) nanoparticles for the delivery of piceatannol,

an anti-cancer drug by ionic gelation method, *Int. J. Pharm., Chem. Biol. Sci.*, 2014, **2**, 12–16.

55 T. Umashankar, M. Govindappa, Y. L. Ramachandra and S. Padmalatha Rai, Channabasava, Isolation and characterization of coumarin isolated from endophyte, alternaria species-1 of Crotalaria pallida and its apoptotic action on HeLa cancer cell line, *Metabolomics*, 2015, **5**, 1–8.

56 A. Vora, A. Riga, D. Dollimore and K. S. Alexander, Thermal stability of folic acid, *Thermochim. Acta*, 2002, **392–393**, 209–220.

57 Y. Qi, M. Jiang, Y. L. Cui, L. Zhao and X. Zhou, Synthesis of quercetin loaded nanoparticles based on alginate for Pb (II) adsorption in aqueous solution, *Nanoscale Res. Lett.*, 2015, **10**, 1–9.

58 K. R. Javed, M. Ahmad, S. Ali, M. Z. Butt, M. Nafees, A. R. Butt, M. Nadeem and A. Shahid, Comparison of doxorubicin anticancer drug loading on different metal oxide nanoparticles, *Medicine*, 2015, **94**, 1–6.

59 S. Srinivasan, V. Bhardwaj, A. Nagasetti, A. Fernandez-Fernandez and A. J. McGoron, Multifunctional surface-enhanced Raman spectroscopy-detectable silver nanoparticles for combined photodynamic therapy and pH-triggered chemotherapy, *J. Biomed. Nanotechnol.*, 2016, **12**, 2202–2219.

60 Y. Wang, B. Newell and J. Irudayaraj, Folic acid protected silver nanocarriers for targeted drug delivery, *J. Biomed. Nanotechnol.*, 2012, **8**, 751–759.

61 S. Balakrishnan, S. Mukherjee, S. Das, F. A. Bhat, P. Raja Singh, C. R. Patra and J. Arunakaran, Gold nanoparticles–conjugated quercetin induces apoptosis via inhibition of EGFR/PI3K/Akt–mediated pathway in breast cancer cell lines (MCF-7 and MDA-MB-231), *Cell Biochem. Funct.*, 2017, **35**, 217–231.

62 C. He, Y. Hu, L. Yin, C. Tang and C. Yin, Effects of particle size and surface charge on cellular uptake and biodistribution of polymeric nanoparticles, *Biomaterials*, 2010, **31**, 3657–3666.

63 M. Nisar, S. A. Khan, M. Qayum, A. Khan, U. Farooq, H. Z. Jaafar, M. Zia-Ul-Haq and R. Ali, Robust synthesis of ciprofloxacin-capped metallic nanoparticles and their urease inhibitory assay, *Molecules*, 2016, **21**, 411.

64 R. Bhanumathi, M. Manivannan, R. Thangaraj and S. Kannan, Drug-carrying capacity and anticancer effect of the folic acid-and berberine-loaded silver nanomaterial to regulate the AKT-ERK pathway in breast cancer, *ACS Omega*, 2018, **3**, 8317–8328.

65 S. A. Sadat Shandiz, M. Shafiee Ardestani, D. Shahbazzadeh, A. Assadi, R. Ahangari Cohan, V. Asgary and S. Salehi, Novel imatinib-loaded silver nanoparticles for enhanced apoptosis of human breast cancer MCF-7 cells, *Artif. Cells, Nanomed., Biotechnol.*, 2017, **45**, 1082–1091.

66 Y. Wang and B. B. Newell, Folic acid protected silver nanocarriers for targeted drug delivery, *J. Biomed. Nanotechnol.*, 2012, **8**, 751–759.

67 S. W. Tsai, J. W. Liaw, F. Y. Hsu, Y. Y. Chen, M. J. Lyu and M. H. Yeh, Surface-modified gold nanoparticles with folic acid as optical probes for cellular imaging, *Sensors*, 2008, **28**, 6660–6673.

68 A. C. Antony, The biological chemistry of folate receptors, *Blood*, 1992, **79**, 2807.

69 J. Sudimack and R. J. Lee, Targeted drug delivery via the folate receptor, *Adv. Drug Delivery Rev.*, 2000, 41.

70 X. Xu, C. Wu, A. Bai, X. Liu, H. Lv and Y. Liu, Folate-functionalized mesoporous silica nanoparticles as a liver tumor-targeted drug delivery system to improve the antitumor effect of paclitaxel, *J. Nanomater.*, 2017, **2017**, 1–13.

71 M. Saad, O. B. Garbuzenko and T. Minko, Co-delivery of siRNA and an anticancer drug for treatment of multidrug-resistant cancer, *Nanomedicine*, 2008, **3**, 761–776.

72 S. H. Tang, R. Li, J. Tan, Y. Wang and Z. T. Jiang, One pot synthesis of water-soluble quercetin derived multifunctional nanoparticles with photothermal and antioxidation capabilities, *Colloids Surf., B*, 2019, **183**, 110429.

73 L. Yang, Y. Liu, M. Wang, Y. Qian, X. Dong, H. Gu, H. Wang, S. Guo and T. Hisamitsu, Quercetin-induced apoptosis of HT-29 colon cancer cells via inhibition of the Akt-CSN6-Myc signaling axis, *Mol. Med. Rep.*, 2016, **14**, 4559–4566.

74 J. Duo, G. C. Ying, G. W. Wang and L. Zhang, Quercetin inhibits human breast cancer cell proliferation and induces apoptosis via Bcl-2 and Bax regulation, *Mol. Med. Rep.*, 2012, **5**, 1453–1456.

75 P. Wang, K. Zhang, Q. Zhang, J. Mei, C. J. Chen, Z. Feng and D. H. Yu, Effects of quercetin on the apoptosis of the human gastric carcinoma cells, *Toxicol. In Vitro*, 2012, **26**, 221–228.

76 S. M. Hussain, K. L. Hess, J. M. Gearhart, K. T. Geiss and J. J. Schlager, *In vitro* toxicity of nanoparticles in BRL 3A rat liver cells, *Toxicol. In Vitro*, 2005, **19**, 975–983.

77 S. C. Boca, M. Potara, A. M. Gabudean, A. Juhem, P. L. Baldeck and S. Astilean, Chitosan-coated triangular silver nanoparticles as a novel class of biocompatible, highly effective photothermal transducers for in vitro cancer cell therapy, *Cancer Lett.*, 2011, **311**, 131–140.

78 H. Chen, L. Shao, T. Ming, Z. Sun, C. Zhao, B. Yang and J. Wang, Understanding the photothermal conversion efficiency of gold nanocrystals, *Small*, 2010, **6**, 2272–2280.

79 D. P. O'Neal, L. Hirsch, N. J. Halas, J. D. Payne and J. L. West, Photo-thermal tumor ablation in mice using near infrared-absorbing nanoparticles, *Cancer Lett.*, 2004, **209**, 171–176.

80 W. Zhang, Z. Guo, D. Huang, Z. Liu, X. Guo and H. Zhong, Synergistic effect of chemo-photothermal therapy using PEGylated graphene oxide, *Biomaterials*, 2011, **32**, 8555–8561.

81 L. Liu, J. Liu, Y. Wang, X. Yan and D. D. Sun, Facile synthesis of monodispersed silver nanoparticles on graphene oxide sheets with enhanced antibacterial activity, *New J. Chem.*, 2011, **35**, 1418–1423.

82 A. Kumar, S. Jha and S. P. Pattanayak, Effect of naringenin on lipids, lipoproteins and lipid metabolising enzymes in 7,12-dimethylbenz(a)anthracene-induced mammary carcinogenesis in SD rats, *Int. J. Pharm. Pharm. Sci.*, 2015, **8**, 154–158.

83 J. M. Argiles and J. Aczon-Bieto, The metabolic environment of cancer, *Mol. Cell. Biochem.*, 1998, **81**, 3–17.
84 S. Leij-Halfwerk, P. C. Dagnelie, J. O. W. van Den Berg, J. D. Wattimena, C. H. Hordijk-Luijk and J. P. Wilson, Weight loss and elevated gluconeogenesisfrom alanine in lung cancer patients, *Am. J. Clin. Nutr.*, 2000, **71**, 583–589.
85 Y. Liu, T. Yin, Y. Feng, M. M. Cona, G. Huang, J. Liu, S. Song, Y. Jiang, Q. Xia, J. V. Swinnen and G. Bormans, Mammalian models of chemically induced primary malignancies exploitable for imaging-based preclinical theragnostic research, *Quant. Imag. Med. Surg.*, 2015, **5**, 708.